Available online at www.sciencedirect.com
ScienceDirect
Journal of Theoretical Biology 251 (2008) 421–439
Journal of Theoretical Biology
www.elsevier.com/locate/yjtbi

Phyllotaxis: Cooperation and competition between mechanical and biochemical processes

Alan C. Newell[a], Patrick D. Shipman[b,c,*], Zhiying Sun[a]

[a]Department of Mathematics, University of Arizona, Tucson, AZ 85721, USA
[b]Department of Mathematics, University of Maryland, College Park, MD 20742, USA
[c]Max Planck Institute for Mathematics in the Sciences, Inselstrasse 22, 04103 Leipzig, Germany

Received 16 May 2007; received in revised form 18 September 2007; accepted 29 November 2007
Available online 8 December 2007

Abstract

Current theories and models of the formation of phyllotactic patterns at plant apical meristems center on either transport of the growth hormone auxin or the mechanical buckling of the plant tunica. By deriving a continuum approximation of an existing discrete biochemical model and comparing it with a mechanical model, we show that the model partial differential equations are similar in form. The implications of this universality in the form of the equations on interpreting the results of simulations are discussed. We develop a combined model that incorporates the coupling of biochemistry and mechanics. The combined model is accessible to analysis by reduction to a set of ordinary differential equations for the amplitudes of shapes associated with both the auxin concentration field and plant surface deformation. Analysis of these amplitude equations reveals the parameter choices under which the two mechanisms may cooperate in determining the pattern, or under which one or the other mechanism may dominate.

Keywords: Phyllotaxis; Auxin; Growth

1. Introduction

Phyllotaxis, namely the arrangement of phylla (leaves, bracts, stickers, florets) on a plant's surface, has intrigued natural scientists for over 400 years. Pictured in Fig. 1 are examples of phylla arranged along ridges (Fig. 1(a)) or spirals (Figs. 1(c,d)). Equally impressive are the related planforms of ridges (Fig. 1(a)), hexagons (Fig. 1(b)), or diamonds (Figs. 1(c,d)) that tile the plant surface.

The challenge is to provide a rational explanation for the formation of such patterns, a mechanism or combination of mechanisms which capture

- the phyllotactic configurations and the reasons for the ubiquitous presence of Fibonacci sequences in spiral phyllotaxis,
- the reasons for the various surface tiling shapes,
- the connection between the phyllotactic configurations and the tiling planforms, and
- the reasons for, and the nature of, transitions which occur in the phyllotactic lattice and planform as a plant grows in size.

Noting that new primordia (when they first form at the shoot apex, phylla are small, undifferentiated bumps on the surface of the plant called primordia) tend to form in the most open space available, Hofmeister (1868) formulated in 1868 a set of rules governing the formation of phyllotactic patterns. These rules, modified over a century later by Snow and Snow (1952), made no reference to the underlying mechanism behind the formation of the primordial bumps, but rather suggested that phyllotaxis can be understood through simple geometric and kinematic laws. The work of Levitov (1991a, b) on the positioning of vortices in superconducting lattices and a series of ingeneous and insightful works by Douady and Couder (1996a) (DC), albeit paradigms, pointed to the idea that

*Corresponding author at: Department of Mathematics, University of Maryland, College Park, MD 20742, USA. Tel.: +1 301 405 5066; fax: +1 301 314 0827.
E-mail addresses: anewell@math.arizona.edu (A.C. Newell), shipman@math.umd.edu (P.D. Shipman).

0022-5193/$ - see front matter © 2007 Elsevier Ltd. All rights reserved.
doi:10.1016/j.jtbi.2007.11.036

Fig. 1. Examples of various phyllotactic lattice and tiling patterns. Ridges (a), undulating ridges (b), hexagons (c), diamonds (parallelograms) (d) and offset diamonds (e) are observed on these succulents. In (d) and (e), the phylla are arranged on families of spirals—families of eight clockwise and 13 counterclockwise spirals in (d) and 13 clockwise and 21 counterclockwise spirals in (e).

phyllotactic configurations minimized some appropriate free energy functional, which in the case of DC was designed to encode the Hofmeister and Snow and Snow rules. As the energy landscape changed with the growing plant, old minima disappeared and new neighboring minima became the new configuration. Many aspects of phyllotactic behavior were captured by these considerations. But not all. The paradigms do not capture ridge-dominated plants (as in Figs. 1(a,b)) or explain the phyllotactic tiling planforms. No physical mechanism for the formation of primordia is suggested by the DC paradigm.

Biophysical mechanisms involving mechanical pressure as the means by which primordia are produced were suggested by Schwendener (1909). Similar ideas are present in the contact pressure models of Airy (1873), Adler (1974), and van Iterson (1907). Within the last 20 years the biomechanical hypothesis has been developed by Green (1999), Green et al. (1998), Dumais and Steele (2000), and Shipman and Newell (2005). Green and colleagues argued that plant growth, and in particular differential growth between the plant corpus and its tunica (outer skin, a layer about 1 or 2 cell layers thick), generates compressive stresses in the tunica and leads to buckling of the plant surface. Experimental backing for this hypothesis includes experimental evidence in sunflowers that compressive stresses are present in the generative region where primordia form (Dumais and Steele, 2000) (although earlier experiments in Snow and Snow, 1951 indicated that the plant surface is under tension, and an extensive study of the stress state of the tunica has not been performed). Additionally, applied mechanical constraints can lead to new leaves (Green, 1999) or altered planforms (Hernández and Green, 1993). The mathematical analysis of Green, Steele and Rennich was primarily a linear one, suggesting how a buckled surface might begin. But, the particular choice, amongst the set of all possible buckling shapes, manifested by the plant is determined by nonlinear interactions, and Green's group was not, apparently, familiar with the seminal work of Koiter (1963) in that regard. Two novel features of that work, emphasized by Shipman and Newell (2004, 2005), are the central roles played both by the quadratic coupling in the nonlinear shell equations and by bias. Quadratic interactions lead naturally to the addition of the arguments of sinusoidal shapes and in particular this leads to the addition of the integer circumferential wavenumbers, a necessary albeit not sufficient, condition for the appearance of Fibonacci, Lucas and double Fibonacci sequences in phyllotactic configurations. Bias, called geometric imperfection by Koiter and continuous bifurcation in the mathematical literature, is important since primordia are formed in an annular region of the plant's shoot apical meristem. Once formed, a primordium moves radially outward into a passive region. It may continue to mature, but it retains its geometrical position relative to the set of all other primordia. As primordia leave the generative region, new primordia are formed in their wake. The lattice of new primordia may be different because the plant has grown and, as we shall see, the plant size is a key parameter in determining phyllotactic configurations. Nevertheless, the old lattice, located on the outer edge of the active, generative region, still has a role to play. It can influence the choice of the configuration which follows by preferentially amplifying certain members of the new set of admissible shapes. This is what we mean by bias. We introduced its effect directly into our quantitative formulation (Newell and Shipman, 2005) and showed how it plays a crucial role in favoring the Fibonacci sequence over alternatives. The role of the plant's phyllotactic history in choosing sequential configurations is also crucial in the DC paradigm.

The role of growth in the mechanical models was, for the most part, passive. To be sure, it was the main reason for the compressive stress in the tunica which can give rise to the buckling pattern. The amplitude of this buckling pattern, however, is of the order of the thickness tunica. Therefore, whereas buckling leads to a template for primordia, it is growth that leads to the visible primordial bumps and phylla. This growth is postulated to be a biochemical response, perhaps through chemical agents such as auxin, to the local stress or curvature inhomogeneities of the buckled surface (Green, 1999).

But chemical models as the initiation mechanism for phyllotaxis also have a long history. The existence of a chemical inhibitor controlling phyllotaxis was proposed by Schoute (1913). Schwabe and Clewer (1984) developed a model for phyllotaxis based on auxin inhibitors. Veen and

Lindenmayer (1977) and Meinhardt (1984) included both activator and inhibitor molecules in reaction–diffusion models. Recent work by the group of Kuhlemeier (Fleming et al., 1997; Reinhardt et al., 2000, 2003; Smith et al., 2006) has made a strong case that the growth hormone auxin and its interaction with the PIN1 transport protein is instrumental in initiating primordia formation. Their evidence includes the following:

1. Auxin transport proteins are essential for primordia formation. When Reinhardt et al. (2000) cultivated shoot apices in the presence of auxin-transport inhibitors, the primordia failed to form. Application of auxin to these meristems resulted in the induction of primordia at the sites of application.
2. Auxin may regulate the expression of the PIN1 transport protein. Vieten et al. (2005) demonstrate that, in the root, PIN proteins are regulated by auxin. Smith et al. (2006) provide evidence for this regulation in the shoot apical meristem.
3. PIN1 is polarized towards incipient primordia. Reinhardt et al. (2003) show that the PIN1 protein is polarized towards incipient primordia. As the primordia are the locations of higher auxin concentration, Smith et al. hypothesize that the polarization is a result of the auxin gradient.

More discussion of the evidence can be found in Smith et al. (2006). This picture has also been supported by mathematical models (Jönsson et al., 2006; Smith et al., 2006; Barbier de Reuille et al., 2006). A key idea in the chemically driven models is the recognition that a uniform auxin concentration can be unstable. What drives the instability? The suggestion is that polarized PIN1 molecules in the cell walls orient themselves according to local auxin concentration. Moreover, they orient themselves so as to facilitate the transport of auxin with its concentration gradient, in effect acting like negative diffusion. This transport can overcome regular auxin diffusion and lead to an instability which enhances the auxin concentration at some locations and depletes it in their immediate neighborhoods.

Such a picture suggests that the surface deformations are passive partners to auxin concentration and are maximal where the phylla are located, slaved to the pattern set by the PIN1-driven uniform auxin concentration instability. Let us emphasize this. The surface deformation of the plant's tunica which we may consider to be an overdamped, curved elastic sheet, is determined by the stresses it experiences. Part of the stress is supplied by the spatially uniform in-surface growth. Another part will be the spatially nonuniform stress distribution triggered by the auxin concentration instability. If the former is not close to the buckling value, the surface deformation will simply be slaved to the latter, resulting in a surface deformation with its maxima at the auxin fluctuation maxima. But we argue that there is ample evidence, including analysis of the relationship between phyllotactic lattice and tiling pattern, to suggest that both mechanisms, auxin/growth localization and nonuniform stress distribution, may play key roles in governing phyllotaxis. It may be that in some plants one mechanism dominates. In others, both mechanisms may be important. It is certainly well known that they are not independent. In biological tissues, growth plays a key role in determining stress distributions (Goriely and Ben Amar, 2005a, b) and it is also known (although the relationship is not well formulated) that stress is key to growth and remodelling (Braam, 2005; Brouzés and Farge, 2004; Shraiman, 2005).

It is very important to note that the shapes of primordia can change as the primorida mature and exit the generative region. For example, the primordia of the cactus in Fig. 1(b) are hexagonally shaped at initiation. These hexagonal shapes evolve into undulating ridges due to secondary growth. Our model only concerns the initiation of primordia in the generative region. The shapes computed by our model must therefore be compared with microscopic images of primordia in the generative region, and caution must be taken in comparing our model results of images of mature phylla as in Fig. 1. However, we suggest that, even upon initiation in the generative region, primordial patterns may show different tiling shapes even if they share the same phyllotactic lattice; see Figs. 6 and 8.

Our goal in this paper is to formulate the interactions and potential competition or cooperation of the two mechanisms. We develop a combined model of stress–strain and growth fields. Through the stress–strain relationship, growth gives rise to compressive stress because of constraints on strain. This is principally seen in an annular region near the shoot apical meristem, the generative region where primordia are formed. Basically, the tunica in the generative region cannot expand in the circumferential direction. A compressive stress, which may be sufficient to initiate a buckling of the plant surface, is the result. Further, any growth inhomogeneities initiated by a nonuniform distribution of auxin also leads to corresponding local stress changes. On the other hand, stress influences growth and we adopt a very simple model for how it does. What we find is that the two mechanisms largely reinforce each other. Moreover, we show that when both the PIN1 transport coefficient and the circumferential growth-induced stress in the plant's generative region are near critical, the cooperation is very strong. What is exciting is that it can lead to phyllotactic patterns and surface deformation patterns which do not match and look substantively different.

The outline of this paper is as follows. In Section 2, we derive a continuum description of the biochemical reaction-transport model of Jönsson et al. (2006). We show that the governing partial differential equation is almost identical in form to that of the buckling model, and indeed to that governing the behavior of a universal class of pattern-forming systems. We introduce a useful coordinization of the fluctuating fields which is more in tune with

what physicists and chemists use to discuss systems in transition. These coordinates are the amplitudes (the order parameters) and wavevectors (the active set) of the shapes of competing configurations. They can be expressed in terms of phyllotactic coordinates. The order parameters for the surface deformation and the growth fields, although coupled, are different. The growth field is assumed to be linearly related to the fluctuation of auxin concentration about its spatially uniform value. Sometimes the coupling leads to the passive enslavement of one set of order parameters to the other but in certain circumstances, which we outline in Section 3, they can be quite independent.

In Section 3, we introduce the combined model. We show how the model is accessible to analysis and leads to the determination of key parameters that dictate the choice of both the phyllotactic lattice and the corresponding planform. In this paper, we focus more on situations in which the biochemical instability sets the phyllotactic pattern in order to illuminate the differing circumstances under which surface deformations mirror and are independent of the growth field configuration. In particular, we find that

(i) The coupling of biochemistry and mechanics can be passive when only one of the mechanisms leads to an instability. In this case, the unstable mechanism dictates the choice of pattern.
(ii) When both mechanisms are close to their instability thresholds, the coupling can be active via a linear resonance. This can lead to ridge-like surface deformations with an underlying whorl lattice (see Fig. 6).
(iii) The coupling can be active via nonlinear resonance. This allows for the formation of various-shaped polygons with an underlying Fibonacci-spiral phyllotactic lattice.

We identify key parameters which should be measured and discuss the sense in which the idea of free energy landscape is still relevant even though in general biochemical systems are not gradient flows.

2. The biochemical model in the continuum limit

A series of pioneering papers by Jönsson et al. (2006), Smith et al. (2006), and Barbier de Reuille et al. (2006) have presented discrete ODE models for the auxin-transport hypothesis of primordium formation. We begin by reexamining these models from a slightly different point of view. Our goal is to take advantage of the fact that the auxin concentration fluctuations found in Jönsson et al. (2006) occur over many cell diameters. We recast the model of Jönsson et al. (2006) using a continuum approximation. This reformulation allows us to examine the combined effects of growth and stress more conveniently.

The idea of a continuum approximation is as follows. Imagine we have a one-dimensional lattice of cells, each of length h_0, and the auxin concentration in the ith cell is $A(i)$, $1 \leqslant i \leqslant N$. We introduce a new field $A(x)$ depending on the continuous variable x, where we identify $A(x = ih_0)$ with $A(i)$. Then, the difference of auxin levels $A(i+1) - A(i)$ in two neighboring cells can be written exactly as $A((i+1)h_0) - A(ih_0) = (\exp(h_0 \frac{\mathrm{d}}{\mathrm{d}x}) - 1)A(x)$. We now expand the exponential in powers of $h_0 \frac{\mathrm{d}}{\mathrm{d}x}$ to get the familiar Taylor series. If $A(i)$ changes significantly over many cell lengths, then powers of $h_0 \frac{\mathrm{d}}{\mathrm{d}x}$ can be estimated as $\frac{h_0}{\lambda}$, where λ is a typical wavelength of the pattern. From simulations (Jönsson et al., 2006), this number is small, at least $\frac{1}{10}$. We keep only terms up to $(h_0 \frac{\mathrm{d}}{\mathrm{d}x})^4$. Why? It turns out that the competition between the reverse diffusion of PIN1 transport and ordinary auxin diffusion is reflected in the second order term, so its coefficient is small near the threshold value for PIN1 transport at which a uniformly distributed auxin concentration becomes unstable. Our series involves a decay term $-dA$, a second order term (in two dimensions) $H_0 h_0^2 \nabla^2 A$, where H_0 is small, and a fourth order term $h_0^4 \nabla^4 A$. The decay rate d (in suitable units) is also small, so that we can have a balance between these three terms such that the neglected sixth and higher derivations are an order of magnitude smaller.

The models used in Jönsson et al. (2006) and Smith et al. (2006) are nonlinear. But, near the value of PIN1 transport at which the pattern first appears, the fluctuations about some mean auxin level (in the cells of the outer surface layer, the tunica) are small. We take advantage of this by expanding the field $A(x)$ around its mean value A_0, $A = A_0(1 + f_0 g)$, and keeping fluctuation terms up to at most cubic order in $f_0 g$. Here, g is the corresponding fluctuation in the amount of strain experienced by the tissue due to a fluctuation $\frac{A - A_0}{A_0}$ in the fractional auxin concentration level. The coefficient f_0 can be interpreted as a coefficient of cubic expansion. The result of all this is a partial differential equation for the auxin fluctuation field $g(x, y, t)$ which reads

$$g_t + D_g \nabla^4 g + H \nabla^2 g + dg + \kappa_1 \nabla(g \nabla g) + \kappa_2 \nabla(\nabla g \nabla^2 g) = 0, \tag{2.1}$$

for

$$D_g = \frac{PTA_0^2 h_0^4}{4(\kappa + A_0)^2},\ H = -h_0^2 D_g + \frac{h_0^2 PTA_0^2}{(\kappa + A_0)^2},\ \kappa_1 = \frac{2PTh_0^2 \kappa A_0}{(\kappa + A_0)^3} f_0,$$
$$\kappa_2 = \frac{PTh_0^4 A_0^2}{2(\kappa + A_0)^3} f_0.$$

The definitions of the parameters will be given in Section 2.1.

The convenience of (2.1) is that it has exactly the form that describes pattern formation in many systems. Moreover, it closely mimics the equation for the normal surface deformation of an overdamped curved elastic shell (for example, in mechanical models of phyllotaxis, the generative region in the neighborhood of the shoot apical meristem) under compressive stresses. This makes it easy to analyze the behavior of the combined model which takes both biochemical and mechanical forces into account.

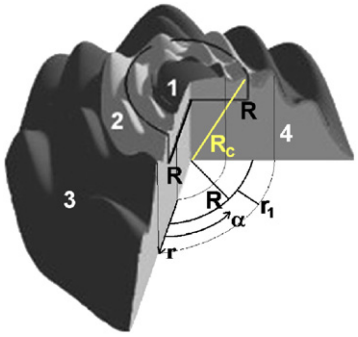

Fig. 2. Schematic diagram of the shoot apical meristem (SAM). The SAM consists of a thin skin (the *tunica*, Regions 1, 2, 3 in the diagram) attached to a foundation of less well-organized cells (the *corpus*, Region 4). Cells in Region 1 show little growth activity and Region 2 is the *generative region* in which some active cell division is occurring and new primordia are first seen to form. As the plant tip grows, cells move from Regions 2 to 3, radially outward in the reference frame of the diagram's north pole. In Region 3, primordia further develop into mature phylla such as leaves. We define radial r and angular α coordinates on the generative region (Region 2) by projecting the surface to polar coordinates on the plane.

The outline of the remainder of this section is as follows. In Section 2.1, we give more details of the derivation of (2.1). The reader may accept this on a first reading and move directly to Section 2.2. In Section 2.2, we discuss how it is that one analyzes the behavior of solutions of (2.1) near onset, that is near the PIN1 transport threshold at which a pattern with some preferred wavelength begins to appear.

In the context of interest, the x, y plane is the annular generative region in the neighborhood of the plant's shoot apical meristem, an average distance R from the apex (see Fig. 2). Thus, for y read r and for x read $R\alpha$, where r and α are, respectively, radial and angular coordinates. (For a generative region near the north pole of a sphere, we define r by projecting the surface in the generative region to the plane; this corresponds more closely to the arc length from the pole for less curved surfaces.) It turns out that the dimensionless ratio $\Gamma = \frac{R}{\Lambda}$, where $2\pi\Lambda$ is the distance between primordia, is relatively large and therefore we can approximate the Laplacian as $\frac{\partial^2}{\partial r^2} + \frac{1}{R^2}\frac{\partial^2}{\partial \alpha^2}$.

2.1. Derivation of the continuum, small fluctuation approximation

In the model of Jönsson et al. (2006), a planar generative region (modelling Region 2 of Fig. 2) in the tunica is taken to be made up of a network, or square lattice, of cells, which we picture in Fig. 3. The auxin concentration $A(i)$ in the ith cell of the lattice is governed by the following set of discrete equations:

$$\frac{dA(i)}{dt} = D_g \sum_k (A(k) - A(i)) + T \sum_k (A(k)P(k,i) - A(i)P(i,k)) + c - dA(i), \quad (2.2)$$

where the above summations are taken over all neighbors of cell i. In Eq. (2.2), $c - dA(i)$ describes the transportation

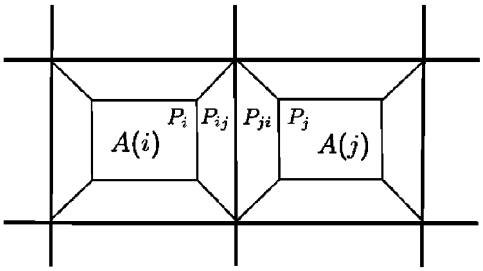

Fig. 3. Schematic diagram of the cell lattice. The lattice of cells is taken to be square lattice. A cell i has auxin concentration $A(i)$ and PIN1 concentration P_i in its interior, and PIN1 concentration P_{ij} on the wall shared with cell j.

of auxin between the meristem top surface and the bulk below. The supply of auxin from the bulk below is characterized by the constant c. When there is excessive auxin in the top surface, it will be transported back down. This is the only part that describes the exchange of auxin between the top surface and the body of the plant. The other two parts both govern the auxin flow inside the generative region. The second part $D_g \sum_k (A(k) - A(i))$ represents normal diffusion. D_g is the diffusion coefficient. The third part $T \sum_k (A(k)P(k,i) - A(i)P(i,k))$ is the so-called PIN1 up-regularization term, because the enzyme PIN1 on the cell wall can polarize so that auxin is transported from low concentration to high concentration, a reverse diffusion. T is a constant measuring the strength of dependency of auxin transportation on the PIN1 distribution. For any k and i, $P(k,i)$ (also denoted as P_{ki}) is the PIN1 concentration on the cell wall of cell k that is adjacent to cell i. The sum $T \sum_k A(k)P(k,i)$ is the amount of auxin flowing into cell i, and $T \sum_k (-A(i)P(i,k))$ is the amount flowing out of cell i.

In order to close Eq. (2.2), a relation between the PIN1 concentration and the auxin concentration is required. Indeed, the PIN1 distribution in a cell is determined by the auxin concentration in the neighboring cells, and this process is called PIN1 cycling. Consider two neighboring cells i and j, with each cell divided into five parts; an internal part, and a four-sided wall. The PIN1 concentration in the internal part is denoted by $P_i = P(i)$, and the PIN1 concentration in cell i on the wall neighboring cell j is denoted by $P(i,j) = P_{ij}$. The time responses of P_{ij} and P_i are taken to be

$$\frac{dP_{ij}}{dt} = f(A(j))P_i - k_2 P_{ij}, \quad (2.3)$$

$$\frac{dP_i}{dt} = \sum_k (k_2 P_{ik} - f(A(k))P_i). \quad (2.4)$$

From Eq. (2.3), we see that the PIN1 concentration on the cell wall (i,j) will increase if a high auxin concentration in cell j calls for more PIN1 to be transported from internal cell i to the cell wall. This effect is represented by the term $f(A(j))P_i$. At the same time, there is also an internalization process $-k_2 P_{ij}$, acting like diffusion, taking PIN1 back to

the internal part of cell i with a constant rate k_2. Similarly, Eq. (2.4) describes the change of PIN1 concentration of the internal part of cell i. The right-hand side of this equation has exactly the opposite sign of Eq. (2.3) because whenever the cell wall loses a PIN1 molecule, the internal cell gains it, and vice versa. Since each cell is surrounded by four sides, a summation is taken over all sides. It is known that $f(A_j)$ is an increasing function of A_j, but the exact formula is unknown. For simplicity, Jönsson et al. assume a linear model, namely that

$$f(A(j)) = k_1 A(j). \tag{2.5}$$

Eqs. (2.3)–(2.5) form a closed system. However, a further and most useful simplification can be made by assuming, consistent with the data given in Table S2 of Jönsson et al. (2006), that the PIN1 relaxation time k_2^{-1} is much less than the auxin concentration relaxation time d^{-1} and that the PIN1 concentration P_{ij} responds adiabatically to changes in $A(i)$. This assumption allow Jönsson et al. to express P_{ki} algebraically in terms of $A(i)$ as

$$P_{ki} = P(k,i) = P\frac{A(i)}{\kappa + \sum_j^{(k)} A(j)}. \tag{2.6}$$

Here $\sum_j^{(k)} A(j)$ is taken over all neighbors of cell k, $P = P_i + \sum P_{ik}$ is the total amount of PIN1 in a single cell and is assumed constant throughout all cells, and $\kappa = \frac{k_2}{k_1}$. Only those PIN1 molecules in the cell walls are of interest because PIN1 molecules in the internal part will not be active in auxin transportation.

From Eq. (2.6), we can see that approximately (exactly if $\kappa \ll \sum A(i)$) the fraction of PIN1 attached to a specific part of cell wall (i,j) is determined by the fraction of auxin concentration in the cell j over the total amount of auxin in neighborhoods of cell i. Substituting Eq. (2.6) into Eq. (2.2), the following closed form of the system of equations for auxin distribution results:

$$\begin{aligned}\frac{dA(i)}{dt} &= D_g \sum_k (A(k) - A(i)) \\ &\quad + T\sum_k \left(A(k)P\frac{A(i)}{\kappa + \sum_j^{(k)} A(j)} - A(i)P\frac{A(k)}{\kappa + \sum_j^{(i)} A(j)} \right) \\ &\quad + c - dA(i) \\ &= D_g \sum_k (A(k) - A(i)) \\ &\quad + TP\sum_k \left(\frac{A(k)A(i)}{\kappa + \sum_j^{(k)} A(j)} - \frac{A(k)A(i)}{\kappa + \sum_j^{(i)} A(j)} \right) \\ &\quad + c - dA(i). \end{aligned} \tag{2.7}$$

These are the equations analyzed by Jönsson et al. (2006). Their results show that for a sufficiently large value of $\frac{PT}{D_g}$, the ratio of reverse to normal diffusion, the spatially uniform solution $A_0 = \frac{c}{d}$ is unstable, and a pattern emerges. The wavelength of this pattern is many cell diameters. Therefore, much simplification can be achieved by recognizing that the solutions $A(i)$ of interest of (2.7) are ones for which $A(i_1 + h_0, i_2 + h_0) - A(i_1, i_2)$ is small. ((i_1, i_2) are the east–west and north–south labels of the ith cell in the square lattice with side length h_0.) Therefore, we can introduce a continuum approximation by replacing the set of concentrations $A(i_1, i_2, t)$, $1 \leqslant i_1, i_2 \leqslant \sqrt{N}$ (N is the total number of cells) by a field $A(x, y, t)$, where $A(x = i_1 h_0, y = i_2 h_0, t) = A(i_1, i_2, t)$. For example, the difference term $D_g \sum_k (A(k) - A(i))$ is written as

$$\begin{aligned} &D_g(A((i_1 - 1)h_0, i_2 h_0) + A((i_1 + 1)h_0, i_2 h_0) \\ &\quad + A(i_1 h_0, (i_2 - 1)h_0) + A(i_1 h_0, (i_2 + 1)h_0) - 4A(i_1, i_2)), \end{aligned}$$

which, when expressed as a Taylor series is, up to fourth order, $h_0^2 D_g \nabla^2 A + D_g \frac{h_0^4}{12} A_4$, where $\nabla^2 = \frac{\partial^2}{\partial x^2} + \frac{\partial^2}{\partial y^2}$ and $A_4 = \frac{\partial^4 A}{\partial x^4} + \frac{\partial^4 A}{\partial y^4}$. The reasons for keeping terms only up to fourth order are discussed above, and the ratio of the first neglected term (the sixth derivative) and the fourth derivative term is estimated below. To expand the PIN1 terms in (2.6), it is convenient to introduce the fractional PIN1 concentration field $G(x, y, t)$, where

$$\begin{aligned} &G(i_1 h_0, i_2 h_0, t) \\ &\quad = \frac{A(i_1, i_2)}{\kappa + A(i_1 + 1, i_2) + A(i_1 - 1, i_2) + A(i_1, i_2 + 1) + A(i_1, i_1 - 1)}. \end{aligned}$$

Then, summing over the four cells adjacent to the ith cell labelled (i_1, i_2),

$$\begin{aligned} &T\sum_k (A(k)P(k,i) - A(i)P(i,k)) \\ &\quad = PTA(i_1, i_2)(G(i_1 + 1, i_2) + G(i_1 - 1, i_2) \\ &\qquad + G(i_1, i_2 - 1) + G(i_1, i_2 + 1)) \\ &\qquad - PTG(i_1, i_2)(A(i_1 + 1, i_2) + A(i_1 - 1, i_2) \\ &\qquad + A(i_1, i_2 - 1) + A(i_1, i_2 + 1)), \end{aligned} \tag{2.8}$$

which, when expanded to fourth order, gives

$$PTh_0^2 \nabla\left(A^2 \nabla\left(\frac{G}{A} \right) \right) + PT\frac{h_0^4}{12}(AG_4 - GA_4). \tag{2.9}$$

Next, we expand about the spatially uniform constant state $A_0 = \frac{c}{d}$ by writing

$$A(x, y, t) = A_0(1 + f_0 g(x, y, t)), \tag{2.10}$$

where f_0 is a coefficient of expansion and the field g is a measure of the auxin fluctuation. (g will be interpreted in Section 3 as the strain induced by a fluctuation $(A(x, y, t) - A_0)/A_0$ in auxin level.) We emphasize that, in this analysis, we are dealing with fluctuations in the auxin concentration which are small with respect to the overall auxin concentration level. The local auxin concentration field $A(x, y, t)$ is certainly never negative. The field $g(x, y, t)$ is a measure of auxin concentration fluctuation. Negative values of g at a given point are possible and just mean that there is an auxin depletion at that point. Substituting (2.8) and (2.9)

into (2.7) and expanding in powers of $f_0 g$ gives

$$\begin{aligned} g_t = & -dg + h_0^2 D_g \nabla^2 g + \frac{D_g h_0^4}{12} g_4 \\ & + PTh_0^2 \left(-\frac{A_0^2}{(\kappa + A_0)^2} \nabla^2 g - \frac{A_0^2 h_0^2}{4(\kappa + A_0)^2} \nabla^4 g \right) \\ & + \frac{PTh_0^4}{12} \left(\frac{A_0 \kappa g_4}{(\kappa + A_0)^2} - \frac{A_0}{(\kappa + A_0)} g_4 \right) \\ & + PTh_0^2 \nabla \left(-\frac{2\kappa A_0 f_0}{(\kappa + A_0)^3} g \nabla g - \frac{h_0^2 A_0^2 f_0}{2(\kappa + A_0)^3} \nabla g \nabla^2 g \right). \end{aligned} \tag{2.11}$$

Observe that the effective diffusion, the coefficient of the Laplacian ∇^2, is

$$-H = -H_0 h_0^2 = h_0^2 \left(D_g - \frac{PTA_0^2}{(\kappa + A_0)^2} \right).$$

For $D_g < PT \frac{A_0^2}{(\kappa + A_0)^2}$, reverse diffusion driven by PIN1 transport overcomes diffusion. If only the Laplacian term were present (if one ignored higher derivatives), an instability of the uniform auxin concentration state $g = 0$ would be possible for $H > 0$ since one could always choose a perturbation with small enough wavelength $\frac{2\pi}{k}$ (that is, large enough wavenumber k) so that the reverse diffusion term $-H\nabla^2 g$ would overcome linear damping $-dg$. But, for larger k, the higher order derivatives become increasingly important and may arrest the linear instability. Their presence leads to a finite choice of the most unstable wavenumber. The fact that the observed pattern is not so big (the pattern wavelength is between 10 and 20 cell diameters) means that, whereas H is positive, it is small. In that case, we note that the g_4 coefficient in (2.11), which is $\frac{h_0^4}{12}(D_g - PT \frac{A_0^2}{(A_0 + \kappa)^2})$, is also small, so that only the rotationally invariant ∇^4 is left in the fourth derivative term.

We can therefore approximate the linear part of the continuum approximation to Eqs. (2.3)–(2.5) by including terms up to the fourth derivative. Because the coefficient H_0 of the Laplacian is small and because (in suitable units) the linear damping is small, the three terms $-dg$, $H_0 h_0^2 \nabla^2 g$ and $D_g \nabla^4 g$ can balance and each of them is larger than the sixth and higher derivative terms which are ignored. An estimate of the ratio of the sixth to fourth derivative terms on a field $\cos \vec{k} \cdot \vec{x}$, $k = |\vec{k}|$, is $\frac{4!}{6!}(h_0 k)^2 \simeq \frac{4\pi^2}{30}(\frac{h}{\lambda})^2$, where λ is the pattern wavelength. For $\frac{h}{\lambda} \simeq \frac{1}{10}$, this ratio is indeed small. As already indicated, we also expand (2.6) around the mean auxin concentration $A_0 = \frac{c}{d}$ as (2.10) and retain all terms to cubic order in the product $f_0 g$. The resulting equation is (2.1).

2.2. Simplification via the use of order parameters

What follows is the standard treatment for pattern-forming systems near onset. A linear analysis of the stability of the uniform solutions $A = A_0$, $g = 0$ can be carried out by setting g proportional to $\exp(\mathrm{i}lr + \mathrm{i}m\alpha)\exp(\sigma t)$ (recall that $\nabla^2 \simeq \frac{\partial^2}{\partial r^2} + \frac{1}{R^2}\frac{\partial^2}{\partial \alpha^2}$ to a good approximation), whereupon

$$\sigma(l, m) = \sigma\left(k^2 = l^2 + \frac{m^2}{R^2} \right) = -D_g k^4 + Hk^2 - d. \tag{2.12}$$

As H increases, the growth rate σ first becomes positive for a value of the wavenumber $k = k_c = \sqrt[4]{\frac{d}{D_g}}$, or $h_0 k_c = \sqrt[4]{\frac{4(\kappa + A_0)^2 d}{PTA_0^2}}$ at the value $H = H_c = 2\sqrt{dD_g}$. Both observations (and the values of the parameters given in Jönsson et al., 2006) suggest an intraprimordial distance $\frac{2\pi}{k_c}$ of between 10 and 15 cell diameters. For H close to H_c, we take $g(r, \alpha, t)$ to be a linear combination of sinusoidal functions with wavevectors $\vec{k} = (l, m)$ in the set $\mathfrak{A}_g$ of wavevectors for which $\sigma(\vec{k})$ is small (positive or negative).

The set $\mathfrak{A}_g$ is the set of wavevectors for the so-called *active modes*. Thus, we write

$$g(r, \alpha, t) = \sum_{\vec{k}_j \in \mathfrak{A}_g} B_j(t) \mathrm{e}^{\mathrm{i}(l_j r + m_j \alpha)} + (*), \tag{2.13}$$

where $(*)$ denotes the complex conjugate of the first term. When convenient, each of the wavevectors $\vec{k}$ in the set can be written in terms of phyllotactic coordinates

$$l = \frac{2\pi}{\lambda_0}(q - md_0), \quad m = m, \tag{2.14}$$

where λ_0 is the plastochrone ratio and $2\pi d_0$ is the divergence angle; see Shipman and Newell (2005) for explanation of the phyllotactic coordinates and the derivation of (2.14). If the lattice is not perfect, but varies in space, we can accommodate this feature in the description by allowing the complex amplitudes $B_j(t)$, called the order parameters, to be slowly varying functions of the spatial variables (see Section 3.6, Remark 11). In (2.14), m is an integer, as is q. The former is the circumferential wavenumber, and the latter measures the number of times the generating lattice corresponding to (2.14) is wrapped around the cylinder $0 < r < \infty, 0 < \alpha < 2\pi$.

The coefficients of all modes with wavevectors $\vec{k}$ for which $\sigma(\vec{k})$ is significantly negative (which we call *passive modes*) are algebraically slaved to the amplitudes of the active modes; that is, the passive modes are algebraic functions of the active modes. The most important nonlinear term is, for small fluctuations, the quadratic nonlinearity. Quadratic interactions between two active modes $\exp(\pm\mathrm{i}(l_p r + m_p \alpha))$ and $\exp(\pm\mathrm{i}(l_q r + m_q \alpha))$ will give an exponential whose exponent contains all sums and differences of the arguments, $\exp(\pm\mathrm{i}(l_p \pm l_q)r + (m_p \pm m_q)\alpha)$. Most of these nonlinearly generated modes will have wavevectors $l_p \pm l_q$, $m_p \pm m_q$ well outside the active set for which $\sigma(l_p \pm l_q, m_p \pm m_q)$ is small. They will not play a role in determining the pattern. On the other hand, a nonlinearly generated phase $-(l_p + l_q)r - (m_p + m_q)\alpha$ for which $\vec{k}_{p+q} = (l_p + l_q, m_p + m_q)$ belongs to the active set $\mathfrak{A}_g$ will lead to a strong interaction between the modes with wavevectors $\vec{k}_p$ $\vec{k}_q$, $\vec{k}_{p+q}$. Standard analysis then yields a set

of amplitude equations

$$\frac{dB_j}{dt} = \sigma(k_j^2)B_j + \sum_{p,q} \kappa(j,p,q)B_p^* B_q^* \tag{2.15}$$

for each of the order parameters B_j in the set $\mathfrak{A}_g$. (We give a detailed derivation of these equations for the mechanical model in Shipman and Newell, 2005.) The coefficient $\kappa(j,p,q)$ (whose nondimensional value is given in Section 3) is only nonzero for triads $\vec{k}_j = -\vec{k}_p - \vec{k}_q$, each of whose wavevectors lie in $\mathfrak{A}_g$.

Amplitude equations such as (2.15) are universal in the sense that they result from the near-threshold analysis of many pattern-forming systems, such as overdamped shells under compressive stress, convection patterns in buoyancy or surface tension-driven unstable fluid layers, Faraday waves in vibrating dishes. The information about the microscopic details is all contained in the coefficients $\sigma(k_j^2)$ and $\kappa(j,p,q)$. The common feature of all the microscopic systems giving rise, near threshold, to the form of (2.15) is simply that they share common symmetries, such as rotational symmetry in the x,y-plane. Therefore, one has to be careful about reaching definite conclusions concerning which mechanism or mechanisms are responsible for the observed pattern. Many different mechanisms which are described by equations such as (2.1) with similar symmetries to (2.1) (here, rotational symmetry and a breaking of the $g \to -g$ symmetry) will give rise to patterns which look similar. To distinguish one mechanism from another, one must see how the pattern behaves as the coefficients σ and κ, which contain information about the particular microscopic model, are changed. The remark applies even before any simplifying reductions of the original equations (2.3)–(2.5) are performed. That Jönnson et al. and Smith et al. note that numerical simulations of Eqs. (2.3)–(2.5) give patterns which are similar to observed phyllotactic patterns cannot be taken as proof that the mechanism giving rise to their model is the correct one. One has to work much harder by showing that the observed changes in pattern which occur as certain external influences are changed are also captured by the model. The same, of course, applies for any mechanical model.

We have already noted that the equations for an overdamped, curved elastic shell under an in-surface compressive stress (possibly induced by the combination of growth and the presence of boundaries which limit expansion) has almost exactly the same form as (2.1). Moreover, near the threshold at which this compressive stress would produce buckling, the surface deformation $w(r,\alpha,t)$ can also be expanded in a set $\mathfrak{A}_m$ of active modes:

$$w(r,\alpha,t) = \sum_{\vec{k}_j \in \mathfrak{A}_m} A_j(t) e^{i(l_j r + m_j \alpha)} + (*), \tag{2.16}$$

and the equations for the order parameters $A_j(t)$ of the surface deformation are the same as (2.15) except for the linear and quadratic coefficients

$$\frac{dA_j}{dt} = \sigma_m(k_j^2)A_j + \sum_{p,q} \tau(j,p,q)A_p^* A_q^*. \tag{2.17}$$

We give the expressions for $\sigma_m(k_j^2)$ and $\tau(j,p,q)$ (derived in Shipman and Newell, 2005) in the next section.

It is very natural to ask, therefore, how the patterns for both the auxin concentration fluctuation ($g(r,\alpha,t)$) and surface deformation ($w(r,\alpha,t)$) fields will interact if we include some coupling between the biochemical and mechanical fields. It is possible that one mechanism dominates in some plants and the other in other plants. For example, while the values for the PIN1 transport may be close to or above threshold, the compressive stress may be well below its threshold value. In that case, the pattern will be set predominantly by the biochemical considerations (the amplitude equations (2.15)) and the coupling will simply slave the surface deformation pattern to the auxin concentration pattern. It is also possible, however, that for other plants the two sets $\mathfrak{A}_g$ (of active modes for the biochemical system) and $\mathfrak{A}_m$ overlap and phyllotaxis will be a cooperation between the two mechanisms. The goal of Section 3 is to examine both of these possibilities.

Before we do that, however, we end this section with a brief discussion of how the solutions $A_j(t)$ and $B_j(t)$ of Eqs. (2.15) and (2.17) can reach finite values. Whereas the quadratic terms redistribute energy amongst the modes, they do not saturate growth. Just as a spherical elastic shell under external pressure will collapse (after first making, for example, a hexagonal pattern), so too will the amplitudes $A_j(t)$ and $B_j(t)$ grow without bound. In the case of the surface deformation, the source of the saturation is fairly clear. The tunica (the curved elastic sheet) is attached to a corpus which acts mechanically as an elastic foundation. This gives rise to spring-like forces in the direction normal to the undeformed surface. In Shipman and Newell (2005), we have modelled this spring force $F(w)$ as a Taylor series $-\kappa w - \gamma_2 w^2 - \gamma_3 w^3$, which leads, in the perturbation analysis, to a slight change in the coefficient $\tau(j,p,q)$ in (2.17) and the addition of cubic terms $-\gamma A_j(|A_j|^2 + 2\sum_{p\neq j}|A_p|^2)$ (γ is a function of γ_2 and γ_3) on the right-hand side of (2.17). Now, strictly speaking, since the linear and quadratic terms balance (that is, they have roughly the same magnitude since the growth σ_m is small), the cubic term will generally be smaller (since it is the third power of the small amplitudes). However, we have argued that γ, the nonlinear restoring coefficient, is likely to be large, and therefore, in (2.17), all three terms will be of the same order of magnitude. The reason for the saturation in (2.15) (which would give rise to cubic terms again having the same form, but different coefficient values, as for (2.17)) is less clear. Certainly the total auxin concentration is bounded, but this fact does not necessarily bound its fluctuations, except, of course, that the concentration cannot be less than zero. Our analysis, however, is looking at situations for which the fluctuation $\frac{A-A_0}{A_0}$ of auxin is

small. One can formally calculate a cubic term, but in order for the cubic term to saturate $B_j(t)$, the amplitudes become large so that higher powers also come into play. We sidestep this issue by simply postulating that the growth fluctuation amplitudes have a saturation $-\delta B_j(|B_j|^2+2\sum_{p\neq j}|B_p|^2)$, where δ is sufficiently large so that all three terms on the right-hand side of (2.15) can balance. But, the cubic saturation term should now be considered phenomenological with the parameter δ determined by the observed fluctuation size.

3. The combination of mechanics and biochemistry

The outline of this section is as follows. First, we will discuss the coupling between the biochemical and mechanical (normal surface deformation and Airy stress potential) fields. Second, we introduce the nondimensionalized equations for these fields. We will state, but not rederive, results from Shipman and Newell (2005) on the Föppl–von Kármán–Donnell (FvKD) equations relevant for this paper. Third, we introduce the order parameter representations of the fields and write down the corresponding coupled set of amplitude equations. Fourth, we analyze the linear growth properties of these equations and identify circumstances in which cooperative rather than dominant behavior by one or the other mechanism can be expected. Fifth, we list 11 important properties of both the linear and nonlinear amplitude equations. We will discuss conditions under which the system is governed by an energy functional (Is there an energy landscape?). Sixth, we review some relevant previous results from Shipman and Newell (2005) valid only when mechanical forces are involved. In that case, it was simply assumed that the local stress inhomogeneities would provide for the growth of phylla to occur at surface deformation maxima. Seventh, we examine three limits of the amplitude equations. Case one corresponds to the case where the auxin concentration field is dominant and the surface deformation observed is simply slaved to the spatial auxin pattern. This case will be of most interest to colleagues who are of the belief that auxin fluctuations are the principal source of phyllotactic patterning. Case two corresponds to the reverse case, where growth-induced in-surface stress effects dominate. The third case is the most interesting because both mechanisms are important. The interesting new result, described in Section 3.7, is that via linear coupling, the surface deformation field and the auxin concentration field (which translates into a growth field) can be very different. Finally, in Section 3.8, we describe how a nontrivial cooperation can take place via nonlinear resonance.

3.1. The coupling of mechanics and biochemistry

To build a simple model that includes mechanics and the effects of auxin, we begin with the stress–strain relations in the generative region of the plant's tunica. Neglecting, for simplicity, and for the moment only, Poisson's ratio, and denoting in-plane stresses (averaged through the width of the tunica) by N_{ij} and (total) strains by ε_{ij}, the stress–strain relations in the angular (α) and radial (r) directions are

$$N_{\alpha\alpha}=Eh(\varepsilon_{\alpha\alpha}-G_{\alpha\alpha}),\quad N_{rr}=Eh(\varepsilon_{rr}-G_{rr}),$$

where E is Young's modulus of the tunica and h its thickness. The functions G_{ij} come from two effects, both consequences of growth. First, they encode plastic, or growth, strains. These strains do not result in stress. If $\varepsilon_{ij}=G_{ij}$, then $N_{ij}=0$. Secondly, the G_{ij} encode stresses EhG_{ij} that arise from restrained growth. Since the plant's annular generative region cannot expand in the circumferential direction (it does a little, as the ring moves outward, but this effect is small), $\varepsilon_{\alpha\alpha}=0$, and a positive $G_{\alpha\alpha}$ gives rise to negative, or compressive, stress. In terms of the stresses N_{ij} and the normal deflection $w(r,\alpha)$ of the tunica shell, the FvKD stress-equilibrium equation (for simplicity, assuming for now that the original shell is flat) reads

$$D\nabla^4 w-N_{rr}\frac{\partial^2}{\partial r^2}w-N_{\alpha\alpha}\frac{1}{R^2}\frac{\partial^2}{\partial\alpha^2}w-2N_{r\alpha}\frac{1}{R}\frac{\partial^2}{\partial r\partial\alpha}w=0, \tag{3.1}$$

where $D=Eh^3\nu^2$, $\nu^2=\frac{1}{12(1-\mu^2)}$ for Poisson's ratio μ, is the bending modulus. In Shipman and Newell (2005), we analyzed the FvKD equation for the case in which $G_{\alpha\alpha}=P/(Eh)$, $G_{rr}=\chi P/(Eh)$ are constant. That is, the growth-induced stresses were assumed to be constant over the generative region. But, the auxin models suggest that growth may not be constant throughout the generative region. To allow for the growth-induced stress to vary spatially, we consider perturbations

$$G_{\alpha\alpha}=\frac{P}{Eh}+g_{\alpha\alpha},\quad G_{rr}=\frac{\chi P}{Eh}+g_{rr},\quad G_{r\alpha}=g_{r\alpha}$$

by functions $g_{\alpha\alpha}(r,\alpha)$, $g_{rr}(r,\alpha)$. Eq. (3.1) then becomes

$$D\nabla^4 w+\chi P\frac{\partial^2}{\partial r^2}w+P\frac{1}{R^2}\frac{\partial^2}{\partial\alpha^2}w-N'_{rr}\frac{\partial^2}{\partial r^2}w-N'_{\alpha\alpha}\frac{1}{R^2}\frac{\partial^2}{\partial\alpha^2}w+2N'_{r\alpha}\frac{1}{R}\frac{\partial^2}{\partial r\,\partial\alpha}w=0,$$

where $N'_{ij}=Eh(\varepsilon_{ij}-g_{ij})$. The next step is to formulate a governing equation for the g_{ij}. Here we make the simplifying assumptions that the tensor $g_{ij}=g\delta_{ij}$ ($g_{rr}=g_{\alpha\alpha}=g, g_{r\alpha}=0$) is isotropic and $g(r,\alpha,t)$ satisfies (2.1) with additional terms added to capture the effects of the fluctuation stress field over the tunica. Defining a perturbation Airy stress function $f(r,\alpha,t)$ by

$$\frac{\partial^2 f}{\partial r^2}=N'_{\alpha\alpha},\quad \frac{1}{R^2}\frac{\partial^2 f}{\partial\alpha^2}=N'_{rr},\quad \frac{1}{R}\frac{\partial^2 f}{\partial r\,\partial\alpha}=-N'_{r\alpha},$$

we take the additional term in (2.2) to be $\beta\nabla^2 f$, where $\nabla^2 f$ is the trace of the stress tensor. Growth is thus enhanced where $\nabla^2 f$ is largest, namely where the total stress $\Sigma=-P-\chi P+\nabla^2 f$ is larger ($\Sigma>0$ implies tension, and $\Sigma<0$ compression). The rationale is that tension (or less compression) allows for plastic stretching of the cell walls. We mention that our formulation of an auxin-induced

growth is similar to that used in the analysis of self-similar wrinkling in leaf edges by Sharon et al. (2007) and Audoly and Boudaoud (2003).

Our combined model then consists of the stress equilibrium equation (3.1) (with an extra term proportional to the curvature of the spherical apex of which the generative region is a part), a compatibility equation that relates f, g, and w, and the biochemical equation (2.1). Written in nondimensional units, the equations are

$$\zeta_m w_t + \nabla^4 w + P\left(\frac{1}{\Gamma^2}\frac{\partial^2}{\partial\alpha^2}w + \chi\frac{\partial^2}{\partial r^2}w\right) + C\nabla^2 f - [f,w] + \kappa w + \gamma w^3 = 0, \tag{3.2a}$$

$$\nabla^4 f + \nabla^2 g - C\nabla^2 w + \tfrac{1}{2}[w,w] = 0, \tag{3.2b}$$

$$\zeta_g g_t + \nabla^4 g + H\nabla^2 g + g + \nabla(\nabla g(\kappa_1 g + \kappa_2\nabla^2 g)) - \beta\nabla^2 f + \delta g^3 = 0. \tag{3.2c}$$

In (3.2), ζ_m and ζ_g are, respectively, relaxation time scales of the overdamped elastic surface and the auxin field, $\Gamma = \frac{R}{\Lambda_g}$, where $2\pi\Lambda_g$, for $\Lambda_g^4 = \frac{D_g}{d}$, is the natural instability wavelength for the critical value of the auxin flux H (namely $H_c = 2$), and C is the nondimensional curvature $\frac{\Lambda_g^2}{R_c vh}$, where R_c is the radius of curvature of the spherical apex and v, h are defined as above. κ and γ are nondimensional spring constants giving the interaction between the plant's tunica and interior. κ and γ are related to their dimensional forms κ' and γ' by $\kappa = \frac{\Lambda_g^4}{D}\kappa'$, $\gamma = \frac{\Lambda_g^4 v^2 h^2}{D}\gamma'$. The natural mechanical buckling wavelength is given by $\Lambda_m^4 = \frac{DR_c^2 v^2 h^2}{D+\kappa' R_c^2 v^2 h^2}$, and defining $L = \frac{\Lambda_g^4}{\Lambda_m^2}$, the constraint $\kappa + C^2 = L$ is satisfied. We take $\nabla^2 = (\frac{1}{\Gamma^2}\frac{\partial^2}{\partial\alpha^2} + \frac{\partial^2}{\partial r^2})$, and the bracket $\Gamma^2[u,v] = \frac{\partial^2 u}{\partial r^2}\frac{\partial^2 v}{\partial\alpha^2} + \frac{\partial^2 u}{\partial\alpha^2}\frac{\partial^2 v}{\partial r^2} - 2\frac{\partial^2 u}{\partial r\,\partial\alpha}\frac{\partial^2 v}{\partial r\,\partial\alpha}$. $[w,w]$ is closely related to the Gaussian curvature of the deformed elastic surface. The surface deformation field w has been scaled by vh and the perturbation Airy stress potential f with D. As explained in Section 3.1, the in-surface growth is accounted for in the term containing second derivatives in (3.2a). If $\chi = 1$, the in-surface stress is equally important in the r and α directions. We shall take $\chi = 0$, as there is experimental evidence to support the idea that the in-plane stress only acts in the α direction (Dumais and Steele, 2000).

We now analyze the behavior of the two coupled fields g and w when one or both of the applied forcing parameters P (compressive stress) or H (PIN1 transport) is close to their critical values $2\sqrt{L}$ and 2, respectively.

3.2. The order parameter equations

As we did in Section 2.2, we represent the fields w and g as linear combinations of sinusoidal functions of the phases

$$\theta_j = l_j r + m_j\alpha,\ j = 1,\ldots,N,$$

$$w, g = \sum_{j=1}^{N}(A_j(t), B_j(t))\,\mathrm{e}^{\mathrm{i}\theta_j} + (*).$$

The wavevectors $\vec{k}_j = (l_j, m_j)$ determine the shapes involved, but it is the relative sizes of the amplitudes—the order parameters $A_j(t), B_j(t)$—which determine the configurations. For example, if $N = 1$, $\vec{k}_1 = (0,m)$, the deformation w is a set of m ribs emanating from the shoot apical meristem. If $N = 3$, $\vec{k}_1 = (0,1)m$, $\vec{k}_2 = (\frac{\sqrt{3}}{2}, -\frac{1}{2})m, \vec{k}_3 = (-\frac{\sqrt{3}}{2}, -\frac{1}{2})m$, and the amplitudes B_1, B_2, B_3 are equal, the auxin concentration field is a hexagonal structure with maxima at the intersections of $\theta_1 = 2n_1\pi$, $\theta_2 = 2n_2\pi$, $\theta_3 = 2n_3\pi$ for integers n_j, $j = 1,2,3$. The common feature of all the members $\vec{k}_j$ belonging to the active set is that one or the other of the corresponding growth rates $\sigma_m(l_j,m_j)$, $\sigma_g(l_j,m_j)$ defined below is small. The amplitudes of the order parameters $A_j(t), B_j(t)$ may not all be of equal size for different $\vec{k}_j$. The order parameter equations are

$$\zeta_m\frac{\mathrm{d}A_j}{\mathrm{d}t} = \sigma_m(l_j,m_j)A_j + CB_j - C\sum\tau_{jpq}A_p^*A_q^* + \sum(\tau'_{qpj}A_p^*B_q^* + \tau'_{pqj}A_q^*B_p^*) - 3\gamma A_j\left(|A_j|^2 + 2\sum_{p\neq j}|A_p|^2\right), \tag{3.3a}$$

$$\zeta_g\frac{\mathrm{d}B_j}{\mathrm{d}t} = \sigma_g(l_j,m_j)B_j + \beta CA_j + \sum\kappa_{jpq}B_p^*B_q^* + \beta\sum\tau'_{jpq}A_p^*A_q^* - 3\delta B_j\left(|B_j|^2 + 2\sum_{p\neq j}|B_p|^2\right), \tag{3.3b}$$

where, for $k^2 = l^2 + \frac{m^2}{\Gamma^2}$,

$$\zeta_m\sigma_m(l,m) = -k^4 + P\frac{m^2}{\Gamma^2} - \kappa - C^2 = -\left(k^2 - \frac{P}{2}\right)^2 + \frac{P^2}{4} - L, \tag{3.4}$$

$$\zeta_g\sigma_g(l,m) = -k^4 + Hk^2 - 1 - \beta = -\left(k^2 - \frac{H}{2}\right)^2 + \frac{H^2}{4} - 1 - \beta, \tag{3.5}$$

and the coefficients $\tau'_{jpq}, \tau_{jpq}, \kappa_{jpq}$ are given by

$$\tau'_{jpq} = \frac{|\vec{k}_p\times\vec{k}_q|^2}{k_j^2} = \frac{(l_pm_q - l_qm_p)^2}{k_j^2\Gamma^2}, \tag{3.6}$$

$$\tau_{jpq} = |\vec{k}_p\times\vec{k}_q|^2\left(\frac{1}{k_j^2} + \frac{1}{k_p^2} + \frac{1}{k_q^2}\right) = \frac{(l_pm_q - l_qm_p)^2}{\Gamma^2}\left(\frac{1}{k_j^2} + \frac{1}{k_p^2} + \frac{1}{k_q^2}\right), \tag{3.7}$$

$$\kappa_{jpq} = \kappa_1 k_j^2 + \kappa_2(\vec{k}_j \cdot \vec{k}_p k_q^2 + \vec{k}_j \cdot \vec{k}_q k_p^2), \tag{3.8}$$

for $k_s^2 = |\vec{k}_s|^2$ and κ_1, κ_2 are defined in (2.1). We note that $\tau_{jpq} = \tau_{pqj} = \tau_{qjp}$ is constant over a triad because $\vec{k}_j + \vec{k}_p + \vec{k}_q = 0$ and that τ'_{jpq} cycled over jpq is τ_{jpq}. If, in addition, the wavelengths $\frac{2\pi}{|\vec{k}|}$ of all participating modes are equal, then all the terms in τ'_{jpq} and κ_{jpq} are equal for all j,p,q permutations. This is because the only wavevectors satisfying $\vec{k}_j + \vec{k}_p + \vec{k}_q = 0$, $|\vec{k}_j| = |\vec{k}_p| = |\vec{k}_q|$, are 120° apart.

The coefficients τ'_{jpq}, τ_{jpq} and κ_{jpq} are nonzero over wavevector triads $\vec{k}_j$, $\vec{k}_p$, $\vec{k}_q$ such that $\vec{k}_j + \vec{k}_p + \vec{k}_q = 0$. The fixed point solutions (we shall see that the flow represented by (3.3) is, to a very good approximation, gradient so that all attracting sets are points which are local minima of some free energy $\mathfrak{E}(A_j, B_j)$) determine the configurations of the vertical deformation and auxin concentration fields. As parameters, and in particular the size parameter Γ, change, so will the fixed points leading to transitions from one surface deformation pattern and phyllotactic lattice to another.

3.3. Linear analysis

We begin with a linear stability analysis of the solution $w = g = 0$ corresponding to uniform auxin concentration and the original tunica surface with no normal deformation. Equivalently, we can look at the linear stability of the solution $A_j = B_j = 0$ of (3.3). Neglecting nonlinear terms in (3.3) and setting $(A_j, B_j) = (\hat{A}, \hat{B})e^{\sigma t}$, we find

$$(\sigma - \sigma_m)\hat{A} = \frac{C}{\zeta_m}\hat{B}, \quad (\sigma - \sigma_g)\hat{B} = \frac{\beta}{\zeta_g} C\hat{A}. \tag{3.9}$$

Eliminating either $\hat{A}$ or $\hat{B}$ in (3.9) gives the growth rate

$$\sigma_\pm = \frac{\sigma_m + \sigma_g}{2} \pm \sqrt{\left(\frac{\sigma_m - \sigma_g}{2}\right)^2 + \frac{\beta C^2}{\zeta_m \zeta_g}}. \tag{3.10}$$

We note that for positive β, σ_+, the larger of the two roots, is always bigger than either σ_m or σ_g. Coupling helps the onset of primordium formation. The curvature of the original surface is important. Fig. 4 shows two graphs of σ_m and σ_g projected on the plane $l = 0$. In Fig. 4(a), we have drawn a situation in which the auxin growth σ_g is about to make a transition from negative to positive while the stress P is small (we make even allow it to be zero or negative), so that σ_m, the buckling growth, is always negative. In this instance, we would expect σ_+ to be dominated by σ_g (it might be useful to think of the coupling growth as being small so that $\sigma_+ \simeq \max(\sigma_g, \sigma_m)$ and for the B_j fields to dominate the A_j fields. Indeed, because σ_m is negative and of order one, the A_j field will be simply slaved to the B_j field through the relation $\sigma_m A_j = -CB_j$. In Section 3.7, we examine this case in more detail. In the same subsection, we will also investigate what happens as P increases so that σ_m increases towards zero. We will find

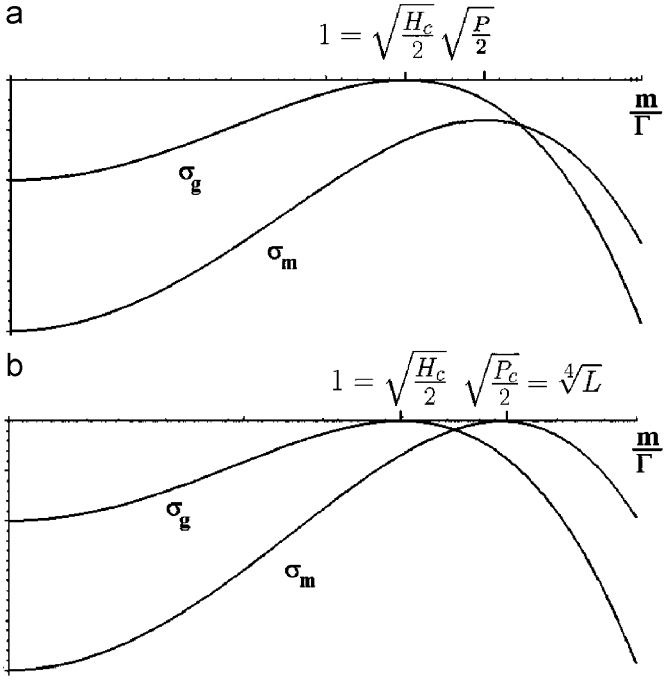

Fig. 4. Graphs of $\sigma_g = -k^4 + Hk^2 - 1 - \beta$ (for $\beta = 0$) and $\sigma_m = -k^4 + Pk^2 - L$, $k^2 = l^2 + \frac{m^2}{\Gamma^2}$ projected on the plane $l = 0$, for (a) $H = H_c$, $P < P_c$ (b) $H = H_c$, $P = P_c$, where $H_c = 2$ and $P_c = 2\sqrt{L}$ are the critical values of H and P.

the slaving tendency of A_j to B_j reduced and the surface deformation will take on a life and shape of its own.

Fig. 4(b) shows a situation where both σ_g and σ_m are close to zero, the former at $\frac{m}{\Gamma} = 1$, and the latter at $\frac{m}{\Gamma} = \sqrt[4]{L}$. If $\sqrt[4]{L}$ is close to 1, there is a strong linear resonance between the two fields. This is examined in Section 3.7. But, one can also have a nonlinear resonance, where $\sqrt[4]{L}$ is such that the cross-coupling terms in (3.2a) (arising from $[\nabla^{-2}g, w]$ in (3.2b) are important). Such a possibility is investigated in Section 3.8.

3.4. Eleven important remarks

1. $\sigma_m(l,m)$ and $\sigma_g(l,m)$ are the growth/decay rates of fluctuations on the separate uniform compression and uniform auxin states in the absence of the other. $\sigma_+(l,m)$ is the modified growth rate in the presence of both. Even in the absence of coupling (i.e., $\beta = 0$), σ_+ is nontrivial. It can be $\sigma_m(l,m)$ for some l,m values and $\sigma_g(l,m)$ for others. It always is the larger of the two.

2. For $\beta > 0$, the case in which the fluctuation stress trace $\nabla^2 f$ produces a positive rate of growth in the field g, σ_+ is always larger than either σ_m or σ_g. Thus, coupling stress and auxin fields enhances primordia formation.

3. σ_g is maximum at on the ellipse $l^2 + \frac{m^2}{\Gamma^2} = \frac{H}{2}$ and, for $\beta = 0$, becomes zero when $H = 2$ (for $\beta > 0$, it becomes zero at $H = 2\sqrt{1+\beta}$, so that $l^2 + \frac{m^2}{\Gamma^2} = 1$. In physical space this corresponds to a wavelength Λ_g, which was used as a nondimensionalization scaling parameter. σ_m is maximum on the ellipse $\chi l^2 + \frac{m^2}{\Gamma^2} = \frac{P}{2}$ and becomes zero when

$P = 2\sqrt{L}$. For $\chi = 0$, this gives that $\frac{m}{\Gamma} = \sqrt[4]{L}$ is the preferred wavenumber.

4. We identify the active set of modes $\mathfrak{A}$ in (3.3) by the criterion that, for a mode $(l, \frac{m}{\Gamma})$, the growth rate $\sigma_+(l,m)$ is greater than some prescribed negative value $-\sigma_+^*$. $-\sigma_+^*$ is not zero since nonlinear coupling can overcome linear damping and lead to stable finite amplitude solutions A_j, B_j. Our results should, however, not be sensitive to the choice of σ_+^* (and they are not).

5. Having identified all possible active modes using linear theory, we now allow them to compete by expanding w and g in an asymptotic expansion with respect to some small parameter (the amount by which σ_+ is above or below critical). The amplitude equations (3.3) are the necessary and sufficient condition that this asymptotic expansion remains well ordered in time.

6. The most important nonlinear terms are the quadratic ones, whereby modes such as $\exp(\pm i\theta_p)$, $\exp(\pm i\theta_q)$, $\theta = lr + m\alpha$, give rise to $\exp(\pm i(\theta_p + \theta_q))$. This coupling produces a resonance with a mode $\exp(i\theta_j)$ already in the active set when $\vec{k}_p + \vec{k}_q + \vec{k}_j = 0$ $(\vec{k}_s = (l_s, \frac{m_s}{\Gamma}))$. For example, let us suppose that

$$\vec{k}_p = \left(l, -\frac{m}{2\Gamma}\right), \quad \vec{k}_q = \left(-l, -\frac{m}{2\Gamma}\right), \quad \vec{k}_j = \left(0, \frac{m}{\Gamma}\right),$$

which encodes a $\frac{m}{2}$-whorl if the amplitudes A_p, A_q, A_j are more or less equal. The choices $l = \frac{\sqrt{3}}{2}$, $\Gamma = m = 4$, give the decussate (2-whorl) pattern. The value of l is chosen by minimizing the elastic energy.

7. It is very important to understand that a ridge solution

$$A_j = \sqrt{\frac{\sigma_m(l_j, m_j)}{3\gamma}}, \quad A_p = A_q = 0$$

is unstable to a configuration with a nonzero A_p, A_q when the quadratic coefficient τ is sufficiently large. Therefore, even though the linear buckling instability leads to radial ridges, the ridges can rapidly destabilize to more hexagonal structures. See Shipman and Newell (2005) for discussion.

8. The cubic terms in (3.3) are not complete. There are many additional terms arising from the interaction of the quadratically generated nonresonant terms in $[w, w]$ with the w field itself. However, we assume that the dominant saturation for the surface deformation is the strong nonlinear elastic foundation term γw^3 and that the saturation of the auxin field is primarily due to a concentration of auxin which is represented in (3.3b) as $\delta B_j(|B_j|^2 + 2\sum_{p\neq j}|B_p|^2)$. Again, our results are relatively insensitive to these choices.

9. We have stated that the fixed generative domain $R - r_1 < r < R + r_1$, $0 < \alpha < 2\pi$, where we consider both R and r_1 large and ignore boundaries, is a simplification. First, the region is moving slowly outwards on those time scales, $\frac{1}{\zeta_m \sigma_+}$ and $\frac{1}{\zeta_g \sigma_+}$, associated with primordia formation. Thus, in reality, we should think that the parameter Γ is a slowly varying function of time. We assume that it is a constant for each calculation of the minimizing configuration $A_j(\Gamma)$, $B_j(\Gamma)$ and then imagine that the amplitudes follow Γ adiabatically. But, the evolution of a given planform with Γ may or may not always be continuous. In Shipman and Newell (2005), we showed that in continuous second-order phase transitions the plant patterns moves up the Fibonacci sequence. Transitions from whorls to spirals are, however, discontinuous.

Second, the pattern moves with the surface material faster than the plant grows. The old pattern passes out of the generative region leaving an unpatterned template on which the next pattern will develop. If Γ increases, the new pattern will have a slightly different structure from the old pattern. Nevertheless, the old one will influence the emerging pattern via its presence on the outer boundary $R + r_1$. This is incorporated into our picture by projecting the shapes of w and g on their outer boundary onto the solvability condition which gives rise to the amplitude equations (3.3). Its effect is to add constants $\bar{A}_j$, $\bar{B}_j$ to each of (3.3a), (3.3b). These additional terms play a central role in the evolving phyllotactic configuration. In Newell and Shipman (2005), we showed how they are key elements in choosing the Fibonacci sequence. The idea, explained in Newell and Shipman (2005), is the following. Suppose one has a spiral pattern with circumferential wavenumbers (the parastichy numbers) $m, n, m+n$, $m < n$, where $m + n \simeq \Gamma$. Quadratic interactions can give rise to modes with circumferential wavenumbers $m+n$ (already present), $2m+n$ (non-Fibonacci if m, n are members of the Fibonacci sequence) or $m+2n$ (Fibonacci). The wavenumber $m+2n$ is preferred since, in forming the boundary, the m mode plays less of a role since it is more strongly damped. As Γ increases past $m+n$ to either $2m+n$ or $m+2n$, the emerging spiral pattern is therefore $n, m+n$, $m+2n$, not $m, m+n, 2m+n$. In fact, because of the first point in this remark, there is a slow evolution from $m, n, m+n$ to $n, m+n, m+2n$. The amplitude A_m decreases as the amplitude A_{m+2n} increases. The in-between pattern displays a surface deformation with amplitudes $A_m \simeq A_{m+2n} \ll A_n \simeq A_{m+n}$, a diamond pattern. What is more intriguing is that the size Γ can be scaled out of the equations altogether. The envelope of the amplitudes, the graph connecting $A_m, A_n, A_{m+n}, A_{m+2n}$, is largely independent of the plant size Γ.

10. An energy functional? It is not a surprise that the amplitude equations for the amplitudes A_j of the vertical deformations can be derived as the gradient $-\frac{\partial \mathfrak{E}}{\partial A_j^*}$ of some energy landscape function $\mathfrak{E}(A_j, B_j)$. The equations were derived from the elastic energy of the generative region. But, the equations for the auxin concentration field, in either their discrete or continuous forms, are not, in general, gradient. There is not a natural functional which optimizes auxin distributions. But, the amplitude equations for B_j are, in special circumstances, gradient. The key is whether the coupling coefficient κ_{jpq} is constant across triads. Its counterpart τ_{jpq}, which is proportional to $|\vec{k}_p \times \vec{k}_q|^2(\frac{1}{k_j^2} + \frac{1}{k_p^2} + \frac{1}{k_q^2})$ is equal to τ_{pqj} and τ_{qjp} because $\vec{k}_j + \vec{k}_p +$

$\vec{k}_q = 0$. But κ_{jpq} is proportional to k_j^2 and $k_j^2(\vec{k}_p \cdot \vec{k}_q)$. This is only constant across the triad if $k_j^2 = k_p^2 = k_q^2 = k^2$ because this, along with the condition that $\vec{k}_j + \vec{k}_p + \vec{k}_q = 0$ means that $\vec{k}_p \cdot \vec{k}_q = \vec{k}_q \cdot \vec{k}_j = \vec{k}_j \cdot \vec{k}_p = -\frac{1}{2}k^2$; namely, the wavevectors are 120° apart in angle. A very similar situation arises in other contexts. Convection in horizontal fluid layers is not a gradient flow. However, as Busse (1967) has shown, near onset it is because the participating wavevectors in triad interactions are equal in length and 120° apart in angle, creating perfect hexagonal lattices. If, in our case, $\kappa_{jpq} = \kappa_{pqj} = \kappa_{qjp} = \kappa$, then the energy functional is

$$\begin{aligned}\mathfrak{E}(A_j, B_j) = & -\sum \sigma_m(\vec{k}_j) A_j A_j^* - \frac{1}{\beta}\sum \sigma_g(\vec{k}_j) B_j B_j^* \\ & - C\sum (B_j^* A_j + B_j A_j^*) \\ & + \frac{C}{6}\sum \tau_{jpq}(A_j A_q A_p + A_j^* A_q^* A_p^*) \\ & - \frac{1}{3}\sum (\tau'_{jpq}(B_j^* A_q^* A_p^* + B_j A_q A_p) \\ & + \tau'_{pqj}(B_p^* A_q^* A_j^* + B_p A_q A_j) \\ & + \tau'_{qjp}(B_q^* A_j^* A_p^* + B_q A_j A_p)) \\ & + \frac{3}{2}\sum (\gamma A_j^2 A_j^{*2} + \frac{\delta}{\beta} B_j^2 B_j^{*2}) \\ & + 3\sum \left(\gamma A_j A_j^* A_p A_p^* + \frac{\delta}{\beta} B_j B_j^* B_p B_p^*\right), \end{aligned} \tag{3.11}$$

and Eqs. (3.3) are $\zeta_m \frac{dA_j}{dt} = -\frac{\partial \mathfrak{E}}{\partial A_j^*}$, $\zeta_g \frac{dB_j}{dt} = -\beta \frac{\partial \mathfrak{E}}{\partial B_j^*}$. The reasons for the factors of $\frac{1}{6}$ and $\frac{1}{3}$ multiplying the cubic terms is that these sums are over all j', p', q' such that $\vec{k}_{j'} + \vec{k}_{p'} + \vec{k}_{q'} = 0$, and a derivation with respect to a fixed j must act on each j', p', q'. A similar remark holds for the factor of 3 on the quartic term. The $\beta \to 0$ limit shows that the growth field decouples. Note that in this limit equation (3.3b) has no terms depending on A_j. If there is an energy functional, we can view the evolution of the plant's surface deformation and phyllotactic lattice as a landscape which evolves as the plant size, measured by Γ, increases. Old minima will disappear and be replaced by new ones. It is easy to picture that sequential minima lie in the same neighborhood of A_j, B_j space. As Γ increases, system (3.3) is going to relax into the nearest minimum accessible to it from its previous positions. That may not, and in fact most often will not, be an absolute minimum of E. In Shipman and Newell (2005), we showed that absolute minima tend to be associated with N-whorl structures. If there is no energy functional, we do not necessarily know that the attractors of (3.3) are stable fixed points. When E exists, we choose the radial wavenumbers l_j by calculating A_j and B_j for different values of the radial wavenumbers and then choosing that set which minimizes the value of E at its local minimum. The corresponding procedure when E does not exist is to choose the radial wavenumbers on the basis of the most stable solution.

11. Modulated patterns. No pattern is a perfect lattice. Moreover, as the plant size increases, there are transitions from one lattice to another. There is a useful way for incorporating such modulations in our description. We will simply state the main idea here; a later work will examine possible outcomes. In order to include a band of wavenumbers in the radial direction, we simply allow the order parameters A_j and B_j to depend slowly on the spatial variable r as well as on time. This introduces diffusion terms proportional to $\frac{\partial^2 A_j}{\partial r^2}$ and $\frac{\partial^2 B_j}{\partial r^2}$ into (3.3) with coefficients that depend on the curvatures of the functions of σ_m and σ_g, defined as functions of l, the radial wavenumber, near their maxima. Solutions of the partial differential equations for the order parameters will admit solutions corresponding to transitions between two different perfect lattice states. Spatially modulated amplitudes will be very useful in allowing us to change slowly the radial wavenumber in the case where we allow the plant size also to be slowly varying.

3.5. A brief review of relevant previous results

It is worthwhile reviewing briefly previous results when only mechanical forces were involved and it was assumed that phylla would simply grow at the maxima of the surface deformation as long as the maxima were isolated. The key results were:

1. The linearly most unstable mode is always purely circumferential. However, for sufficiently strong quadratic coupling, the purely circumferential mode is unstable to a three mode structure. The ratios of the amplitudes of the other two modes and the amplitude of the circumferential of the stationary state increases with the ratio of quadratic to linear coefficients.
2. The quadratic coefficient τ_{jpq} in (3.3) arising from the strain elastic energy is maximum when one of its radial wavenumbers is zero. This means that this coefficient is a sensitive function of the divergence angle d_0 and prefers values of d_0 which are ratios of next to consecutive members of the Fibonacci sequence. Also, the balance between the linear growth rate σ_m and τ ensures that the radial wavenumbers of the other two participating modes in the triad are order one.
3. When $\Gamma = 2N$, absolute minima are achieved for three mode structures with circumferential wavenumbers N, $N, 2N$. When Γ increases to $2N + 1$, the preferred structure has circumferential wavenumbers, $N, N + 1$, $2N + 1$.
4. Fibonacci sequences appear because if P is sufficiently supercritical, more than one triad can compete. For example, if one begins with a 2, 3, 5 structure with $\Gamma = 5$ and then lets Γ increase, it is possible for the wavevectors $\vec{k}_7 = \vec{k}_2 + \vec{k}_5$ and $\vec{k}_8 = \vec{k}_3 + \vec{k}_5$ to compete. The coefficient of the quadratic terms A_2A_5 and A_3A_5 are maximized when $d > \frac{2}{5}$ and $d < \frac{2}{5}$, respectively. In almost all circumstances and very much because of the

bias on the outer boundary of the radial region provided by the 3 and 5 modes (the 2 mode is more strongly damped), the latter wins and the new stationary state is a combination of the four modes $\vec{k}_2, \vec{k}_3, \vec{k}_5, \vec{k}_8$, with corresponding amplitudes $A_2 \simeq A_8 < A_3 \simeq A_5$ which leads to a diamond shape. As Γ continues to increase, the participating modes are $\vec{k}_2, \vec{k}_3, \vec{k}_5, \vec{k}_8, \vec{k}_{13}$ and the amplitudes $A_2 \simeq A_{13} < A_3 \simeq A_5 < A_8$. All these transitions are second order and d_0 changes continuously towards the golden angle value.

5. The shape of the graph of the amplitudes A_j is invariant as Γ increases (see Shipman and Newell, 2005, Fig. 28).

A later paper will discuss the extension of these results to the case where biochemistry is included. For the remainder of this paper, however, our goal is to illustrate with two examples how the two mechanisms can cooperate and in particular to demonstrate the nontrivial connection between the phyllotactic lattice, namely the lattices of auxin maxima and the corresponding surface deformations and tilings.

3.6. Four cases

Now that we have laid the groundwork, we proceed to some new results which accentuate the role that auxin can play in forming the plant surface and phyllotactic arrangements. We are guided by the graphs of the individual growth functions $\sigma_m(l,m)$ and $\sigma_g(k)$ and their composite $\sigma_+(l,m)$, as shown in Fig. 4. We discuss four different cases.

Case 1: Auxin dominates. In Fig. 4(a), we show the surfaces $\sigma_g(l,m)$, $\sigma_m(l,m)$ projected on the plane $l=0$. The value of the PIN1 transport has reached the critical level $H_c = 2$ and the auxin distribution is about to become unstable to the wavenumber $(l^2 + \frac{m^2}{\Gamma^2})^{1/2} = 1$. The auxin fluctuation amplitudes B_j will be determined from (3.3b). The corresponding surface deformation mode amplitudes A_j will be slaved to the auxin fluctuation amplitudes B_j by $\zeta_m \sigma_m(l_j, m_j) A_j = -CB_j$. The surface deformation will look very similar to the auxin deformation.

Case 2: The compressive stress dominates. This is the opposite of case 1. For $l = 0, \frac{m}{\Gamma} = 1 \simeq \sqrt{L}$, σ_m is about to cross-zero for the circumferential mode $\vec{k}_1 = (0,1)$ so that $m = \Gamma$. As we have shown in Shipman and Newell (2005), for τ sufficiently large, the circumferential mode will be unstable to modes with nontrivial radial structures $\vec{k}_2 = (-l, \frac{m}{2\Gamma})$, $\vec{k}_3 = (l, \frac{m}{2\Gamma})$. The resulting $\frac{m}{2}$-whorl will drive the slaved auxin concentrations $\zeta_g \sigma_g(0,m) B_1 = \beta C A_1$, $\zeta_g \sigma_g(0, \frac{m}{2}) B_j = \beta C A_j$, $j = 2,3$. Here, and in the following, we write $\sigma_g(0,m)$ for $\sigma(\vec{k}_3 = (0, \frac{2N}{\Gamma}))$.

Case 3: Cooperation. Linear resonance. From this case, we can also understand the outcomes of cases 1 and 2. Both growth functions $\sigma_m(l,m)$ and $\sigma_g(l,m)$ have maxima in common and the values of both PIN1 transport and the circumferential compressive stress are close to their critical values. Fig. 4(b) shows the projections of σ_m and σ_g on the plane $l=0$. We examine this in Section 3.7.

Case 4: Cooperation. Nonlinear resonance. The two fields are also coupled through the nonlinear terms in Eqs. (3.2a) and (3.2b). In Section 3.8, we examine how this nonlinear coupling can lead to different lattice-planform combinations.

3.7. Anatomy of an N-whorl. Cooperation, linear resonance

We now illustrate these ideas by examining the transition between cases 1 and 3. We investigate the anatomy of an N-whorl phyllotactic pattern as the in-surface induced compressive stress P increases from a value for which $\sigma_m = -0.5$ to 0. The change in-surface geometry is dramatic (Fig. 6).

By an N-whorl we mean a phyllotactic lattice pattern in which primordia form in groups of N elements equidistant from the center of the plant, equidistant to each other, and offset by an angle $2\pi d_0 = \frac{2\pi}{2N}$ from the previously formed primordia. N-whorls are produced by the wavevector choices $\vec{k}_{2N} = (0, \frac{2N}{\Gamma})$, $\vec{k}_N^{++} = (l, -\frac{N}{\Gamma})$, $\vec{k}_N^{--} = (-l, -\frac{N}{\Gamma})$ for $l = \frac{\sqrt{3}}{2}$ (see Shipman and Newell, 2005). We imagine that auxin is the main instigator of the phyllotactic system and choose $m = \Gamma = 2N$ and $\sigma_g(k) = 0$ so that the three modes are $\vec{k}_{2N} = (0,1)$, $\vec{k}_N^{++} = (l, -\frac{1}{2})$, $\vec{k}_N^{--} = (-l, -\frac{1}{2})$. We begin by taking $\beta = 0$ so that growth is unaffected by local stress changes. In this case, there is an exact hexagonal solution $|B_{2N}| = |B_N^+| = |B_N^-| = b$ for (3.3b). We then calculate the corresponding amplitudes A_{2N}, A_N^+, A_N^- for the surface deformation. We take $\sigma_m(l, -N) = \sigma_m(-l, -N) = -0.5$ and examine the ratios $\frac{|A_N^+|}{|A_{2N}|}$ as $\sigma_m(0, 2N)$ is increased from -0.5 to 0. The results are shown in Fig. 5(a), and the plant surface and phyllotactic lattice for $N = 6$ are drawn in Fig. 6. We note the following very important conclusion. For $\sigma_m(0, 2N) = -0.5$, strongly negative, the ratios

$$\frac{|A_N^+|}{|A_{2N}|} = \frac{|A_N^-|}{|A_{2N}|} = 1,$$

and the surface deformation has the same hexagonal shape as that of the auxin concentration field. But, as $\sigma_m(0, 2N)$ approaches zero, the mechanical buckling instability takes on a life of its own. The surface deformation amplitudes are no longer linearly slaved to the auxin concentration field, but involve their nonlinear terms in (3.3a). We note that, as $\sigma_m(0, 2N)$ evolves from -0.5 to 0, the above ratio of amplitudes decreases from 1 to 0.25. The resulting surface deformation is strongly ridge-like (see Fig. 6). This pattern continues as we increase the coupling of stress and growth by increasing β from zero to finite values. The results are shown in Fig. 5(b,c). Again, as $\sigma_m(0, 2N)$ approaches zero, the surface deformation is more ridge-like although the parameter β means that the local stress and growth are more strongly coupled at the linear level.

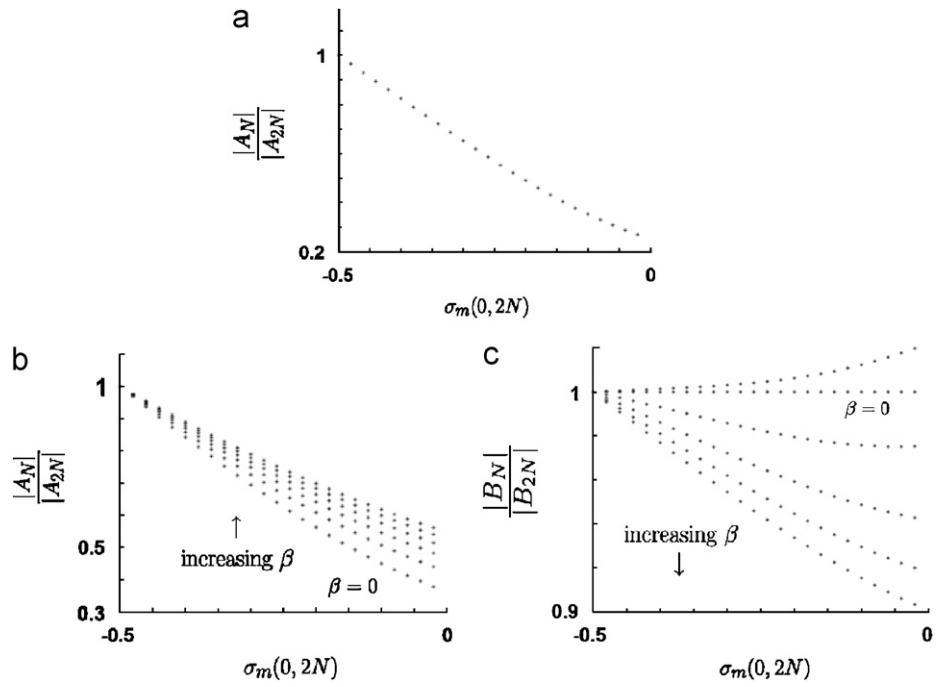

Fig. 5. (a) As described in the text, the amplitudes A_N^+, A_N^-, A_{2N} are found for the case $\beta = 0, C = 0.4, \kappa = 0.25, \gamma = \frac{1}{15}, L = 1$. Plotted is the ratio $|A_N^+|/|A_{2N}| = |A_N^-|/|A_{2N}|$ as a function of $\sigma_m(0, 2N)$. (b,c) The effect of the biochemical–mechanical coupling coefficient β on the amplitude ratios. For β increasing from 0 to positive values, the amplitude ratios $|A_N^+|/|A_{2N}|$ and $|B_N^+|/|B_{2N}|$ are plotted as functions of $\sigma_m(0, 2N)$. Other parameters are as for part (a).

Thus, it is not at all contradictory for plants to display a phyllotactic lattice configuration (the arrangement of phylla on the surface) which is very different in appearance from the surface deformation. The auxin concentration and surface deformation fields share the same geometry (the same $\vec{k}_j$'s), but their amplitude ratios are different.

In the simulations of Figs. 5 and 6, the curvature parameter C is taken to be $C = 0.3 > 0$. Positive (respectively negative) C correspond to a convex (respectively concave) apical meristem and $C = 0$ to a flat apical meristem. Without the coupling to an auxin field, we found in Shipman and Newell (2005) that $C < 0$ is required for positive amplitudes A_j of the surface deformation; for $C > 0$ the mechanical energy-minimizing amplitudes A_j were found to be negative, and the resulting surface deformation is one in which the centers of the phylla are the minima, not the maxima of the surface. In the simulations reported here, the positive amplitudes B_j allow for stable solutions with $A_j > 0$ even with $C > 0$. This is important, since although C might indeed be negative in many cactus meristems, most plant meristems are convex.

3.8. Cooperation. Nonlinear resonance

In Shipman and Newell (2004, 2005), we showed that, as the plant grows, its phyllotactic pattern is governed by overlapping triads $\vec{k}_m, \vec{k}_n, \vec{k}_{m+n}, \vec{k}_{m+2n}, \ldots$ whose circumferential wavenumbers are sequential members of the Fibonacci sequence (see Remark 9). We now reexamine this scenario when both mechanical buckling and auxin redistribution processes are in play. The new result again illustrates the importance of amplitudes in determining what is observed. We choose the simple case $\beta = 0$ so Eqs. (3.3b) for the biochemical amplitudes B_j decouple from the mechanical amplitudes A_j. The energy $\mathfrak{E}(A_j, B_j)$ in (3.11) does not apply when $\beta = 0$, but the B_j-amplitude equations are the variations $\frac{dB_j}{dt} = -\frac{\partial}{\partial B_j}\mathfrak{E}_B$ of the energy

$$\mathfrak{E}_B(B_j) = -\sum \sigma_g(\vec{k}_j) B_j B_j^* - \kappa \sum (B_j^* B_p^* B_q^* + B_j B_p B_q) + \frac{3}{2}\delta \sum \beta B_j B_j^* + 6\delta \sum (B_j B_j^* B_p B_p^*). \tag{3.12}$$

$\mathfrak{E}_B(B_j)$ is the limit of $\beta\mathfrak{E}(A_j, B_j)$ as β tends to zero. This energy only applies for the symmetric case $\kappa = \kappa_{jpq} = \kappa_{pqj} = \kappa_{qjp} = \kappa$. We will allow for wavevector choices for which this condition does not hold, and to solve the equations we approximate the coefficient κ_{jpq} by a constant κ. Our strategy, then, is to find an $\mathfrak{E}_B$-energy-minimizing choice of wavevectors $\vec{k}_j$ and corresponding amplitudes B_j. These values of $\vec{k}_j$ and B_j are then used in the A_j-amplitude equations (3.3a) to find the amplitudes A_j. Physically, this corresponds to an auxin-transport instability determining a *patterned*, *nonuniform* stress state which can then lead to a buckling instability with the same underlying phyllotactic lattice (encoded in the choice of $\vec{k}_j$), but possibly a different amplitude distribution and therefore different tiling planform.

In contrast to the previous discussion of whorls, we now allow for multiple triads of wavevectors favored by the nonlinear interactions. We include the eight wavevectors

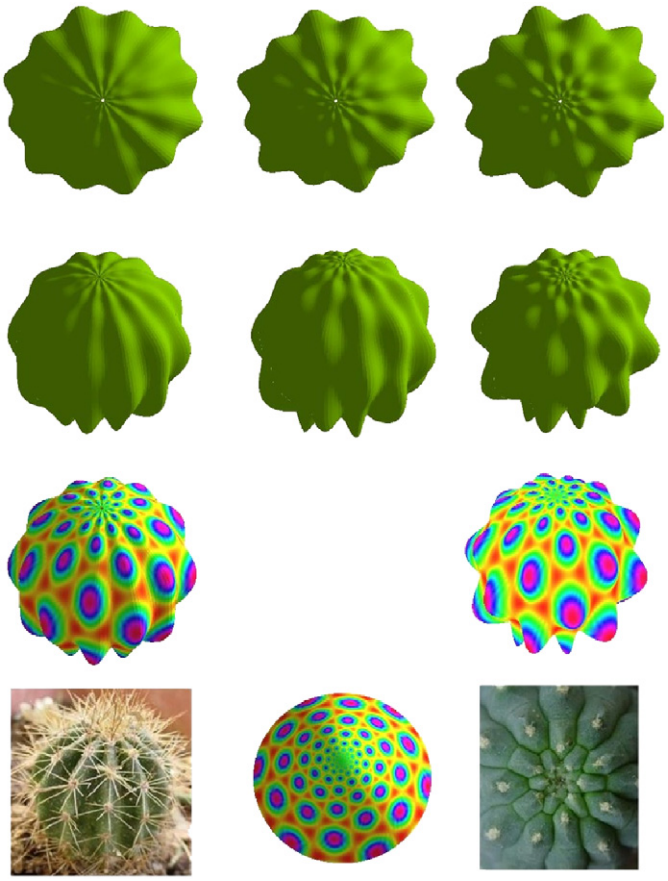

Fig. 6. The surface deformation and auxin distribution corresponding to the experiments of Fig. 5(a). In the top two rows, the deformation $w = A_6^+ \cos(lr + 6\alpha) + A_6^- \cos(-lr + 6\alpha) + A_{12}\cos(12\alpha)$ is plotted as a deformation of the sphere for $A_6^{\pm}/A_{12} = \frac{1}{3}$ (first column, corresponding to $\sigma_m = 0$ in Fig. 5(a)), $A_6^{\pm}/A_{12} = \frac{2}{3}$ (second column, corresponding to $\sigma_m = -\frac{1}{3}$ in Fig. 5(a)) and $A_6^{\pm}/A_{12} = 1$ (third column, corresponding to $\sigma_m = -\frac{1}{2}$ in Fig. 5(a)). The auxin distribution is plotted in the third row together with the surface deformation and in the center of the fourth row by itself; plotted is $g = B_6^+ \cos(lr + 6\alpha) + B_6^- \cos(-lr + 6\alpha) + B_{12}\cos(12\alpha)$ with $B_6^+ = B_6^- = B_{12}$. Pictured also in the fourth row are plants that show similar surface deformations.

$\vec{k}_3, \vec{k}_5, \vec{k}_8 = \vec{k}_3 + \vec{k}_5, \vec{k}_{13} = \vec{k}_5 + \vec{k}_8, \vec{k}_{21} = \vec{k}_8 + \vec{k}_{13}, \vec{k}_{34} = \vec{k}_{13} + \vec{k}_{21}, \vec{k}_{55} = \vec{k}_{21} + \vec{k}_{34}, \vec{k}_{89} = \vec{k}_{34} + \vec{k}_{55}$, where

$$\vec{k}_3 = \left(\frac{2\pi}{\lambda_0}(1 - 3d_0), \frac{3}{\Gamma}\right), \quad \vec{k}_5 = \left(\frac{2\pi}{\lambda_0}(2 - 5d_0), \frac{5}{\Gamma}\right).$$

For a given choice of Γ and H slightly above critical, we find the values of the divergence angle $2\pi d_0$ and plastochrone ratio λ_0 and the amplitudes $B_3, B_5, \ldots, B_{89}$ that minimize the energy (3.12). For $\Gamma \simeq 19$ and $H = 2.4 = H_c + 0.4$, we find $d_0 = 0.3816$ (close to the golden angle $2\pi d_0 = 2\pi(0.3819662...)$) and the amplitudes B_j graphed in Fig. 7. These values and Eq. (3.3a) then determine the amplitudes A_j, and the surface deformations are graphed in Fig. 8.

Of particular interest is the parameter $L = \frac{\Lambda_g^4}{\Lambda_m^4}$ measuring the ratio of natural biochemical Λ_g and mechanical Λ_m wavelengths. For $L = 1$, the amplitudes A_j match the

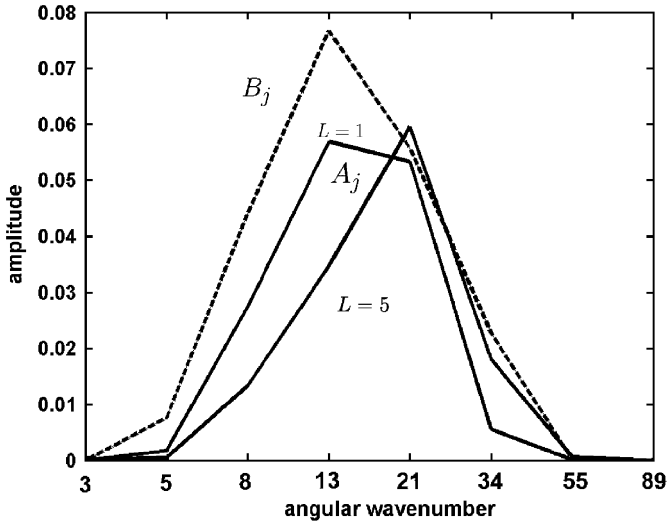

Fig. 7. The amplitudes A_j, B_j (vertical axis) vs. angular wavenumber. The amplitude equations for eight modes with angular wavenumbers $3, 5, \ldots, 89$ are solved as described in the text for the parameter values $\Gamma = 19.2$, $H = 2.4$, $\kappa = 3$, $\delta = 0.01$, $C = 1$, $\gamma = 0.01$, $\chi = 0$ and (i) $L = 1$, $P = 2.4$, or (ii) $L = 5$, $P = 6$. Plotted are the amplitudes B_j (dotted line) and the amplitudes A_j (solid lines).

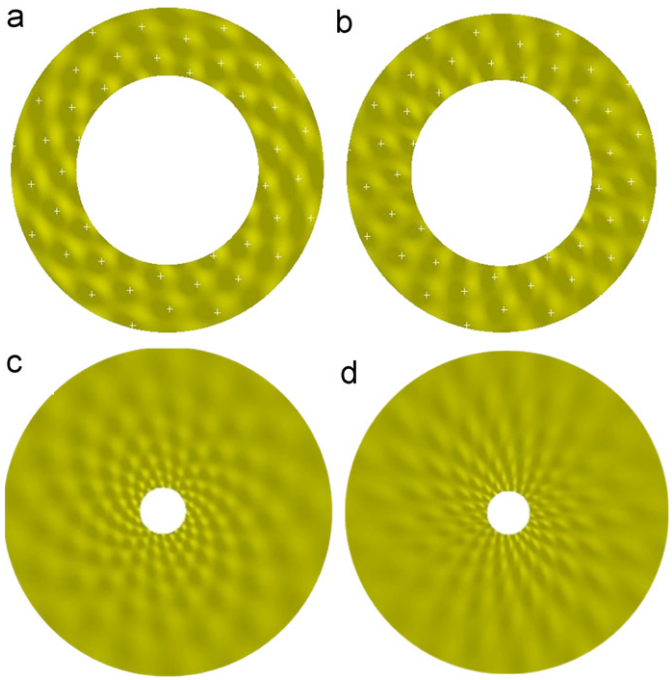

Fig. 8. Simulations of surface deformations corresponding to the experiment of Fig. 7. Graphed are the surface deformations $w(s, \alpha)$ for (a,c) $L = 1$, (b,d) $L = 5$; (a,b) for the plastochrone difference ($s = r$); (c,d) with the plastochrone ratio ($s = \ln(r)$). In (a,b), the phyllotactic lattice corresponding to the maxima of the deformation is marked by white crosses; both figures display the same lattice.

amplitudes B_j; in both cases, the amplitude corresponding to angular wavenumber $n = 13$ is the largest; see Fig. 7. This results in a configuration of diamond-shaped phylla as shown in Fig. 8(a,c). For $L = 5$, the favored biochemical

wavelength is $\sqrt[4]{5} \simeq 1.5$ times the favored mechanical wavelength, and the amplitudes A_j are maximized at angular wavenumber $n = 21$. The resulting surface deformation is that of elongated (relative to the case $L = 1$) diamond-shaped phylla. These results are robust and not sensitive to the choice of parameters δ, γ, κ, and C.

4. Discussion

In this paper, we have shown that existing models for the two proposed mechanisms for phyllotactic pattern formation—auxin transport and mechanical buckling—have governing equations that are very similar in form but differ in the interpretation of parameters. Both sets of equations determine an instability to periodic deformations of a given natural wavelength as a bifurcation parameter—either the auxin-transport parameter H or the compressive stress P—increases above a critical value. And, both models are accessible to analysis by the reduction to amplitude equations that are universal in form but contain information about the microscopic mechanism in their coefficients. In particular, the coefficients σ_g and σ_m of the linear terms in the amplitude equations determine the set of active modes that participate in the determination of the pattern, whereas the coefficients κ_{jpq} and τ_{jpq} of the quadratic terms bring into play triad interactions that are important for the formation of lattice structures.

The universal form of the amplitude equations highlights the fact that the results of any model must be interpreted with care. As emphasized in the introduction, it is not enough to obtain results that mimic real plants; the results must lead to testable predictions and determination of key parameters or combinations of parameters. What predictions result from our combined auxin-mechanical model? Let us review the results. The coupling between mechanics and biochemistry can be either passive or active and involve both linear and nonlinear terms in the equations. Therefore, different outcomes involving the relationship between the chosen phyllotactic lattice and the corresponding planform are possible.

Cases 1/2: If either auxin transport or compressive stress dominates as the critical instability-driving mechanism, then that mechanism determines the phyllotactic lattice (the wavevectors $\vec{k}_j$) and also the corresponding amplitudes. The amplitudes for the other mechanism are slaved and match those of the dominant mechanism. The dominant mechanism therefore determines both the phyllotactic lattice and the tiling planform.

Case 3: If the compressive stress and auxin-transport parameters P and H are both near critical, cooperation between the two mechanisms can occur through the linear terms in the equations. In this case, a set of wavevectors $\vec{k}_j$ is chosen, but the corresponding amplitudes B_j of the auxin distribution may not match the amplitudes A_j of the buckling configuration. In particular, we show in Fig. 6 how N-whorls with $B_N^+ = B_N^- = B_{2N}$ but ridge-like surface deformation amplitudes $A_N^+ = A_N^- \ll A_{2N}$ may arise.

Case 4: The cooperation between the two mechanisms may occur through the nonlinear terms in the equations. This results in Fibonacci-like planforms which involve multiple triads of wavevectors driven by the nonlinear terms. Key to understanding the relation between the phyllotactic lattice and the tiling planform is the parameter $L = \frac{\Lambda_g^4}{\Lambda_m^4}$, giving the ratio of biochemical to mechanical natural wavelengths. We show in Fig. 8 how diamond-shaped phylla or elongated diamond phylla are preferred depending on how close L is to 1. For $L = 1$, we are close to a linear resonance.

The relative sizes of the parameters P and H and their proximity to their critical values thus distinguishes between cases 1/2, in which one mechanism dominates, and the cooperative cases 3/4. Nonlinear cooperation (case 4) and the related diamond-shaped planforms are favored by large quadratic coefficients τ_{jpq} and κ_{jpq} which bring in the nonlinear interactions. The mechanical coefficient τ_{jpq} is proportional to the curvature of the buckling surface; one expects therefore a larger nonlinear effect on a more curved apical meristem. The biochemical quadratic coefficient κ_{jpq} is, in general, not symmetric over permutations of j, p, q due to the fact that the biochemical system is not the gradient of an energy. However, for certain wavevector choices, including those that are associated with N-whorl configurations, κ_{jpq} is symmetric and the system is then gradient. In our simulations, we approximated κ_{jpq} by a constant and therefore studied a gradient system, but a deeper understanding of the role of a nongradient system in determining the choice of pattern is desired. Still lacking is an understanding the relationship between gradient or nongradient PDE models and the energy-landscape approach to phyllotaxis central to the work of Levitov (1991a, b), Douady and Couder (1996a, b), Atela et al. (2002), and Hotton et al. (2006).

We should also comment on how the continuum approximation developed here can complement the discrete model of Jönnson et al. A discrete model has the advantage of directly capturing the fact that cells are discrete objects. One consequence of going to a continuum model is that we need to introduce a cubic saturation term and parameter δ into the amplitude equations to achieve finite-amplitude solutions. In the discrete model, it is enough to assume that there is fixed amount of total auxin to prevent an infinite amount of auxin from accumulating in a cell. However, Jönnson et al. also note that their simulations tend not to give stable patterns. It is not clear from the discrete model if this is due to how the cells are connected or if the model is nongradient. Both effects may be important, but our continuum approximation reveals that the model is nongradient due to the asymmetry of the quadratic coefficient as a function of the wavevectors. There is no reason to expect that a biochemical mechanism would be gradient, but the form of the quadratic terms in the discrete model (coming from the relation (2.6)) still needs experimental justification. We note that Heisler and Jönsson (2006)

introduced the effects of an additional chemical to produce stable patterns; alternatively they could have modified the system to make it gradient.

The continuum approximation has two main advantages. First, as discussed above, it reveals the universality in the form of the suggested model and the presence of quadratic terms which produce triad interactions. Note that Smith et al. (2006) choose a quadratic dependence of auxin flux on auxin concentration to give optimal control over spacing of primordia in their model. This quadratic dependence is not based on experiment, but rather on designing a model that gives optimal results. Secondly, the continuum approximation allows one to identify the combinations of parameters that contribute to the coefficients of the linear or quadratic terms in the equations. As previously mentioned, it is not reproducing patterns, but identifying the coefficients that change the competition between various patterns that distinguishes between a model that only contains the correct symmetries of the physical problem and a model that is based on the right microscopic details. These coefficients have not been identified in the model of Smith et al., for example, who note that many parameters need to be changed to go from one pattern to another.

We have suggested that models of phyllotaxis must be able to account not only for the phyllotactic lattice, but also for the corresponding tiling planforms. And, our model shows the potential for various tiling planforms with a single underlying lattice. The relation between lattice and planform has, however, not received much attention in the biological literature. Williams (1975), following Richards (1951) observes that the same phyllotactic lattice may be interpreted as one that exhibits, for example, families of five and eight spirals if the phylla are circumferentially elongated, or as one that exhibits families of eight and 13 spirals if the phylla are radially elongated. It is important to extend these observations to the shapes of primordia in the generative region.

An understanding of the relationship between lattice and tiling shape is further complicated by the fact that part of the phyllotactic pattern may be set before one actually observes the deformation of the surface. The development of a primordium, from the initial determination of sites of elevated auxin concentration, to the development of a well-defined unit, includes many biochemical and biophysical processes operating at different length and time scales. In this paper, we have considered only two of these processes. The universality of the governing equations, however, suggests that similar sets of coupled equations, differing in the physical interpretation of the parameters, may describe other biochemical or mechanochemical interactions.

The presence of compressive stress in the tunica of the generative region has only been shown in sunflowers. In our model, a mechanical instability is possible if the pressure P of the uniform compressive stress is well below critical, and, in fact, for large enough B_j, even if P is zero or negative. Thus, even if the plant cell walls are generally under tension, mechanics may play a role in patterning. A similar scenario is suggested by Fleming (2006). Stress could also play a role directly in the PIN1-auxin interaction. Note that the experimental evidence that auxin up-regulates PIN1 orientation is weak; this is concluded from the fact that PIN1 is oriented towards primordia centers, where there is a larger auxin concentration. PIN1 could also be regulated by stress as the stress state differs in primordium centers.

The simulations in this paper were made for a fixed value of the nondimensionalized meristem radius Γ. We have discussed, however, how the choice of whorl or Fibonacci-spiral patterns is influenced by the bias of previously formed configurations on newly forming configurations and the importance of transitions between patterns as Γ changes. How transitions can be understood in an amplitude-equation approach is discussed in our previous work with a mechanical model (Shipman and Newell, 2005; Newell and Shipman, 2005). Understanding the effects that cooperation between mechanics and biochemistry can have on transitions between patterns will be the subject of future work.

Acknowledgements

This work is supported by NSF Grant number DMS-0501243. PS is supported by an NSF Postdoctoral Fellowship Grant DMS-0503196. We thank Alain Goriely for very useful discussions.

References

Adler, I., 1974. A model of contact pressure in phyllotaxis. J. Theor. Biol. 45, 1–79.
Airy, H., 1873. On leaf arrangement. Proc. R. Soc. 21, 176.
Atela, P., Golé, C., Hotton, S., 2002. A dynamical system for plant pattern formation: rigorous analysis. J. Nonlinear Sci. 12 (6).
Audoly, B., Boudaoud, A., 2003. Self-similar structures near boundaries in strained systems. Phys. Rev. Lett. 91, 086105.
Barbier de Reuille, P., Bohn-Courseau, I., Ljung, K., Morin, H., Carraro, N., Godin, C., Traas, J., 2006. Computer simulations reveal properties of the cell–cell signaling network at the shoot apex in Arabidopsis. Proc. Natl Acad. Sci. 103, 1627–1632.
Braam, J., 2005. In touch: plant responses to mechanical stimuli. New Phytol. 165, 373–389.
Brouzés, E., Farge, E., 2004. Interplay of mechanical deformation and patterned gene expression in developing embryos. Curr. Opinion Genet. Dev. 14, 367–374.
Busse, F.H., 1967. On the stability of two-dimensional convection in a layer heated from below. J. Math. Phys. 46, 140–150.
Douady, S., Couder, Y., 1996a. Phyllotaxis as a dynamical self-organizing process, Part I: the spiral modes resulting from time-periodic iterations. J. Theor. Biol. 178, 255–274.
Douady, S., Couder, Y., 1996b. Phyllotaxis as a dynamical self-organizing process, Part II: the spontaneous formation of a periodicity and the coexistance of spiral and whorled patterns. J. Theor. Biol. 178, 295–312.
Dumais, J., Steele, C.R., 2000. New evidence for the role of mechanical forces in the shoot apical meristem. J. Plant Growth Regul. 19, 7–18.
Fleming, A.J., 2006. Leaf initiation: the integration of growth and cell division. Plant Mol. Biol. 60, 905–914.

Fleming, A.J., McQueen-Mason, S., Mandel, T., Kuhlemeier, C., 1997. Induction of leaf primordia by the cell wall protein expansion. Science 276.

Goriely, A., Ben Amar, M., 2005a. Differential growth and instability in elastic shells. Phys. Rev. Lett. 94, 198103.

Goriely, A., Ben Amar, M., 2005b. Growth and instabilities in elastic tissues. J. Mech. Phys. Solids. 53, 2284–2319.

Green, P.B., 1999. Expression of pattern in plants: combining molecular and calculus-based paradigms. Am. J. Bot. 86.

Green, P.B., Steele, C.S., Rennich, S.C., 1998. How plants produce patterns. A review and a proposal that undulating field behavior is the mechanism. In: Jean, R.V., Barabé, D. (Eds.), Symmetry in Plants. World Scientific, Singapore, pp. 359–392.

Heisler, M.G., Jönsson, H., 2006. Modeling auxin transport and plant development. J. Plant Growth Regul. doi: 10.1007/s00344-006-0066-x.

Hernández, L.H., Green, P.B., 1993. Transductions for the expression of structural pattern: analysis in sunflower. Plant Cell 5, 1725–1738.

Hofmeister, W., 1868. Allegmeine Morphologie der Gewachse, Handbuch der Physiologischen Botanik. Engelmann, Leipzig.

Hotton, S., Johnson, V., Wilbarger, J., Zwieniecki, K., Atela, P., Golé, C., Dumais, J., 2006. The possible and the actual in phyllotaxis: bridging the gap between experimental observations and iterative models. J. Plant Growth Regul. 25, 313–323.

van Iterson, I., 1907. Mathematische und Mikroskopisch-Anatomische Studien über Blattstellungen nebst Betrachtungen über den Schalenbau der Miliolinen. Gustav Fischer, Jena.

Jönsson, H., Heisler, M.G., Shapiro, B.E., Meyerowitz, E.M., Mjölsness, E., 2006. An auxin-driven polarized transport model for phyllotaxis. Proc. Natl Acad. Sci. 103, 1633–1638.

Koiter, W.T., 1963. Proc. K. Ned. Akad. Wet. B Phys. Sci. 66, 263.

Levitov, L.S., 1991a. Energetic approach to phyllotaxis. Europhys. Lett. 14, 533–539.

Levitov, L.S., 1991b. Phyllotaxis of flux lattices in layered superconductors. Phys. Rev. Lett. 66, 224–227.

Meinhardt, H., 1984. Models of Biological Pattern Formation. Academic Press, London.

Newell, A.C., Shipman, P.D., 2005. Plants and Fibonacci. J. Stat. Phys. 121 (5–6), 937–968.

Reinhardt, D., Mandel, T., Kuhlemeier, C., 2000. Auxin regulates the initiation and radial position of lateral organs. Plant Cell 12, 501–518.

Reinhardt, D., Pesce, E.-R., Stieger, P., Mandel, T., Baltensperger, K., Bennett, M., Traas, J., Friml, J., Kuhlemeier, C., 2003. Regulation of phyllotaxis by polar auxin transport. Nature 426, 255–260.

Richards, F.J., 1951. Phyllotaxis: its quantitative expression and relation to growth in the apex. Philos. Trans. R. Soc. B 235, 509–564.

Schoute, J.C., 1913. Beiträge zur Blattstellungslehre I. Die Theorie. Rec. Trav. Bot. Neerl. 10, 153–339.

Schwabe, W.W., Clewer, A.G., 1984. Phyllotaxis—a simple computer model based on the theory of a polarly-induced inhibitor. J. Theor. Biol. 109, 595–619.

Schwendener, S., 1909. Theorie der Blattstellungen. Sitzungsber. Akad. Wiss. Berlin 741–773.

Sharon, E., Roman, B., Swinney, H.L., 2007. Geometrically-driven wrinkling observed in free plastic sheets and leaves. Phys. Rev. E 75, 046211.

Shipman, P.D., Newell, A.C., 2004. Phyllotactic patterns on plants. Phys. Rev. Lett. 92 (16), 168102.

Shipman, P.D., Newell, A.C., 2005. Polygonal planforms and phyllotaxis on plants. J. Theor. Biol. 236, 154–197.

Shraiman, B.I., 2005. Mechanical feedback as a possible regulator of tissue growth. Proc. Natl Acad. Sci. 102.

Smith, R.S., Guyomarc'h, S., Mandel, T., Reinhardt, D., Kuhlemeier, C., Prusinkiewicz, P., 2006. A plausible model of phyllotaxis. Proc. Natl Acad. Sci. 103, 1301–1306.

Snow, M., Snow, R., 1951. On the presence of tissue tension in apices. New Phytol. 50, 185–484.

Snow, M., Snow, R., 1952. Minimum areas and leaf determination. Proc. R. Soc. B 139, 545–566.

Veen, A.H., Lindenmayer, A., 1977. Diffusion mechanism for phyllotaxis, theoretical, physico-chemical and computer study. Plant Physiol. 60, 127–139.

Vieten, A., Vanneste, S., Wisniewska, W., Benková, E., Benjamins, R., Beeckman, T., Luschnig, C., Friml, J., 2005. Functional redundancy of PIN proteins is accompanied by auxin-dependent cross-regulation of PIN expression. Development 132, 4521–4531.

Williams, R.F., 1975. The Shoot Apex and Leaf Growth. Cambridge University Press, Cambridge.